Geophysical Journal International

Geophys. J. Int. (2016) **207,** 1554–1572
Advance Access publication 2016 September 20
GJI Marine geosciences and applied geophysics

doi: 10.1093/gji/ggw352

Fully anisotropic 3-D EM modelling on a Lebedev grid with a multigrid pre-conditioner

Piyoosh Jaysaval,[1,*] Daniil V. Shantsev,[2] Sébastien de la Kethulle de Ryhove[3] and Tarjei Bratteland[3]

[1]*Department of Physics, University of Oslo, P.O. Box* 1048 *Blindern,* 0316 *Oslo, Norway. E-mail: piyoosh.jaysaval@fys.uio.no*
[2]*EMGS, I&I Technology Center, P.O. Box* 2087 *Vika,* 0125 *Oslo, Norway*
[3]*EMGS, I&I Technology Center, P.O. Box* 1878 *Lade,* 7440 *Trondheim, Norway*

Accepted 2016 September 19. Received 2016 September 15; in original form 2015 December 2

SUMMARY

We present a numerical algorithm for 3-D electromagnetic (EM) simulations in conducting media with general electric anisotropy. The algorithm is based on the finite-difference discretization of frequency-domain Maxwell's equations on a Lebedev grid, in which all components of the electric field are collocated but half a spatial step staggered with respect to the magnetic field components, which also are collocated. This leads to a system of linear equations that is solved using a stabilized biconjugate gradient method with a multigrid preconditioner. We validate the accuracy of the numerical results for layered and 3-D tilted transverse isotropic (TTI) earth models representing typical scenarios used in the marine controlled-source EM method. It is then demonstrated that not taking into account the full anisotropy of the conductivity tensor can lead to misleading inversion results. For synthetic data corresponding to a 3-D model with a TTI anticlinal structure, a standard vertical transverse isotropic (VTI) inversion is not able to image a resistor, while for a 3-D model with a TTI synclinal structure it produces a false resistive anomaly. However, if the VTI forward solver used in the inversion is replaced by the proposed TTI solver with perfect knowledge of the strike and dip of the dipping structures, the resulting resistivity images become consistent with the true models.

Key words: Numerical solutions; Electrical anisotropy; Electromagnetic theory; Marine electromagnetics.

INTRODUCTION

Marine controlled-source electromagnetic (CSEM) surveying is an important technique for hydrocarbon exploration (Eidesmo *et al*. 2002; Ellingsrud *et al*. 2002; Constable 2010). The technique uses a high-powered electric dipole source to probe subsurface resistivities and has proven to be very useful for detecting resistive hydrocarbon reservoirs, which often show up as anomalies in CSEM data and in its inversion results (see e.g. Hesthammer *et al*. 2010; Fanavoll *et al*. 2012; Alcocer *et al*. 2013).

A reliable inversion and interpretation of CSEM data in complex tectonic environments with varying anisotropy remains one of the major challenges in the hydrocarbon exploration industry. This is primarily due to shortage of efficient 3-D forward modelling codes that can accurately calculate the electric and magnetic fields in complex anisotropic conductivity structures. In inversion and interpretation of industrial CSEM data, anisotropy of the Earth is either ignored or (most often) simplified as vertical transverse isotropy (VTI). The VTI assumption is only valid if the subsurface consists of horizontal sedimentary layers having a vertical axis of symmetry. In complex tectonic settings, however, the subsurface may have dipping sedimentary layers, which results in tilted transverse isotropic (TTI) media with tilted axes of symmetry. For example, typical geological structures necessary for hydrocarbon accumulation such as an anticline, a syncline, an overthrust, or tilted layers near salt domes could produce an effective TTI medium with a large inclination of axis of symmetry. The simplified assumption of VTI anisotropy in such complex tectonic areas may result in a misleading interpretation of EM data. For example, Li & Dai (2011) and later Davydycheva & Frenkel (2013) studied the effect of tilted anisotropy on synthetic CSEM responses, respectively, for 2.5-D and 3-D problems and concluded that ignoring such anisotropy in CSEM data interpretation might be the core reason for some false-negative and false-positive EM anomalies.

In order to get reliable inversion results in complex tectonic areas, key requirements are therefore to have an accurate anisotropic

*Now at: The University of Texas at Austin, Institute for Geophysics, Austin, TX, USA.

forward modelling algorithm as well as an inversion scheme that can employ this modelling algorithm. In the past, some 3-D anisotropic forward modelling algorithms have been developed, for example by Weidelt (1999), Wang & Fang (2001), Weiss & Newman (2002), Davydycheva *et al*. (2003) and Liu & Yin (2014). However, to our knowledge, there have been no published reports on either CSEM inversion schemes that can handle arbitrary anisotropy (or at least TTI), or studies of the possible effect of TTI anisotropy on results obtained by conventional inversion with VTI assumption. In this paper, we develop a forward modelling algorithm for media with general anisotropy and use this in an inversion scheme to perform a comparative study of inversion results obtained with the VTI assumption of the model anisotropy against those obtained with the TTI assumption.

The finite-difference (FD) method is a commonly used approach to simulate EM responses. In the FD method, the governing partial differential equations (PDEs) are usually discretized on a staggered Yee grid (Yee 1966); see for example the FD algorithms developed by Newman & Alumbaugh (2002), Streich (2009) and Jaysaval *et al*. (2015). These algorithms are based on a simplified assumption stating that the anisotropic media can be described by only three diagonal elements of the 3×3 conductivity tensors (e.g. VTI, horizontal transverse isotropic [HTI], or triaxial anisotropic media). In a standard Yee grid, the electric field components are located at the middle of the cell edges, while the magnetic field components are located at the centres of the cell faces, and no electric or magnetic field component is collocated with any other field component. The basic Yee approach suits well for the simple case of the diagonal conductivity tensor, but it is not easily generalized to an arbitrary anisotropic medium, which is described by 3×3 conductivity tensors with non-zero off-diagonal elements. In such media, the anisotropic Ohm law relates each component of the current density with all three components of the electric field. Therefore, discretization of Maxwell's equations requires values for all electric field components at each electric field node of the FD grid.

In order to extend an FD algorithm based on the Yee grid to handle an arbitrary anisotropic media, one can interpolate all electric field components at each electric field node from their values on neighbouring nodes; see for example Weidelt (1999), Wang & Fang (2001), Weiss & Newman (2002) and Liu & Yin (2014). However, such interpolation may result in a number of drawbacks as outlined by Davydycheva *et al*. (2003) and Davydycheva & Frenkel (2010). To list a few among these, the interpolation effectively doubles the size of FD cell and can lead to loss of the current conservation property in the grid cells: the ingoing and outgoing currents may not be equal. Thus, the interpolation scheme can significantly reduce the accuracy of the FD method. Besides, the inverse of a local interpolation operator cannot be local, which can be troublesome, for example, it will destroy the duality between the electric and magnetic fields.

An alternative FD method for arbitrary anisotropic media is to use the so-called Lebedev grid (Lebedev 1964). In this grid, all electric field components are collocated at one set of nodes and all magnetic field components are collocated at another set of nodes. This ensures that there is no need for interpolation, and hence no loss of the current conservation property in the grid cells. The Lebedev-grid FD approach for EM modelling was implemented in the frequency domain by Davydycheva & Druskin (1999) and Davydycheva *et al*. (2003), and in the time domain by Nauta *et al*. (2013). The Lebedev grid can be decomposed into four shifted Yee grids. Consequently, the computation cost increases fourfold as compared to the Yee grid. At the same time, as demonstrated by Davydycheva *et al*. (2003) the Lebedev grid exhibits improved error cancellation properties, and thus allows using coarser cell sizes.

The forward modelling using the FD discretization of frequency-domain Maxwell's equations, on either a Yee or a Lebedev grid, leads to a system of linear equations. For realistic EM simulations, the resulting linear system is sparse, but very large and may involve up to several millions of unknowns. Such a linear system can be efficiently solved using sparse direct solvers, see Streich (2009), da Silva *et al*. (2012), Jaysaval *et al*. (2014) and Puzyrev & Koric (2015), but they are very demanding in terms of memory and flops requirements. Therefore, one often uses iterative solvers that are computationally less demanding. The most frequently used group of iterative solvers are based on Krylov subspace methods; see for example Newman & Alumbaugh (1995), Smith (1996), Druskin *et al*. (1999), Puzyrev *et al*. (2013), Börner *et al*. (2015) and the references therein. The convergence of Krylov methods depends on the condition number of the linear system: the smaller the condition number, the faster the convergence. For EM applications, the system may be poorly conditioned, and hence the use of Krylov methods requires special preconditioners to accelerate the convergence (Saad 2003).

An efficient preconditioner can be obtained using multigrid methods (Wesseling 1991; Briggs *et al*. 2000; Trottenberg *et al*. 2001), which are among the fastest iterative solution techniques known today. For 3-D EM modelling, Aruliah & Ascher (2002) have presented a multigrid preconditioner for Krylov methods for the finite-volume discretization of Maxwell's equations. Mulder (2006) has implemented a multigrid method as a standalone solver as well as a preconditioner for Krylov methods for the finite-integration (FI) discretization of Maxwell's equations. In both papers, the discretization is based on the staggered Yee grid. Koldan *et al*. (2014) have recently presented an algebraic multigrid preconditioner for Krylov solvers for the finite-element (FE) implementation of Maxwell's equations. However, the multigrid methods have not yet been applied for linear systems obtained from the discretization of Maxwell's equations on the Lebedev grid.

In this paper, we present a Lebedev-grid based FD modelling with a multigrid preconditioner for simulating EM fields in arbitrary 3-D anisotropic media. The resulting linear system is solved using a Krylov subspace based preconditioned biconjugate-gradient-type method, for example BiCGStab(2) (van der Vorst 1992; Gutknecht 1993). Computation of a multigrid preconditioner involves determination of a number of different components: a set of grids with different degrees of coarseness, intergrid transfer operators and a so-called smoother (Trottenberg *et al*. 2001). All these components have been implemented for the Lebedev grid, following the similar ideas as in Mulder's (2006) implementation for the Yee grid. The smoother is based on the method introduced by Arnold *et al*. (2000), who locally solved small linear systems at nodes of the grid cells. This smoother takes care of the large null-space of the 3-D curl-curl operator, and hence avoids the requirement of an explicit divergence correction as proposed by Smith (1996).

The developed forward solver for 3-D media with general anisotropy is then used to demonstrate that assuming a simplified VTI anisotropy in inversion and interpretation of industrial CSEM data can lead to erroneous conclusions. For this, a synthetic inversion study is performed by considering 3-D resistivity models with anticlinal and synclinal structures from Davydycheva & Frenkel (2013). We first present inverted resistivity images obtained by a VTI inversion, which uses a forward solver assuming a VTI anisotropy, and show that the simplified VTI assumption can lead to misleading inversion results. We then replace the VTI solver

by the proposed forward solver that can handle TTI anisotropy of the models, and obtain resistivity images that are consistent with the true resistivity models.

The paper is divided into four main sections. We first describe the EM modelling in general 3-D anisotropic media. We provide details of the FD discretization of the governing PDEs on the Lebedev grid. This is followed by the theory and implementation of the multigrid method, which we use as a preconditioner to a BiCGStab(2) solver. We subsequently benchmark our numerical results using layered (1-D) and 3-D TTI earth models. Finally, we examine the effect of tilted anisotropy on synthetic inversion results before drawing concluding remarks.

ANISOTROPIC FD EM MODELLING

Assuming a temporal-dependence of $e^{-i\omega t}$ with the angular frequency ω, a vector Helmholtz equation for the electric field can be derived from Maxwell's equations in the quasi-static limit. Following Jaysaval *et al.* (2014, 2015), we have

$$\nabla \times \nabla \times \mathbf{E}(\mathbf{r}) - i\omega\mu\bar{\boldsymbol{\sigma}}(\mathbf{r})\mathbf{E}(\mathbf{r}) = i\omega\mu\mathbf{J}(\mathbf{r}). \quad (1)$$

Here $\mathbf{r} \equiv x\hat{\mathbf{x}} + y\hat{\mathbf{y}} + z\hat{\mathbf{z}}$ is the position vector, $\mathbf{E} \equiv E_x\hat{\mathbf{x}} + E_y\hat{\mathbf{y}} + E_z\hat{\mathbf{z}}$ and $\mathbf{H} \equiv H_x\hat{\mathbf{x}} + H_y\hat{\mathbf{y}} + H_z\hat{\mathbf{z}}$ are, respectively, the electric and magnetic field vectors, $\mathbf{J} \equiv J_x\hat{\mathbf{x}} + J_y\hat{\mathbf{y}} + J_z\hat{\mathbf{z}}$ is the electric current density vector of a transmitter, and μ is the magnetic permeability. The value of μ is assumed to be constant and equal to the free space value $\mu_0 = 4\pi \times 10^{-7}\mathrm{Hm}^{-1}$. The term $\bar{\boldsymbol{\sigma}}\mathbf{E}$ is the Ohmic conduction term and describes induced current density in the conductive Earth. $\bar{\boldsymbol{\sigma}}(\mathbf{r})$ is a symmetric 3×3 electric conductivity tensor and takes the form

$$\bar{\boldsymbol{\sigma}} = \begin{bmatrix} \sigma_{xx} & \sigma_{xy} & \sigma_{xz} \\ \sigma_{yx} & \sigma_{yy} & \sigma_{yz} \\ \sigma_{zx} & \sigma_{zy} & \sigma_{zz} \end{bmatrix} \quad (2)$$

in an arbitrary anisotropic medium, where the elements of $\bar{\boldsymbol{\sigma}}$ relate the components of the current density and electric field such that $J_x = \sigma_{xx}E_x + \sigma_{xy}E_y + \sigma_{xz}E_z$, and similarly for J_y and J_z. For brevity, hereinafter the dependency on the position vector $\mathbf{r}$ is omitted. The off-diagonal elements of $\bar{\boldsymbol{\sigma}}$ are zero for isotropic, VTI, HTI or triaxial anisotropic medium.

Using the definition of the curl operator in eq. (1), we obtain

$$\partial_y\partial_x E_y - \partial_y^2 E_x - \partial_z^2 E_x + \partial_z\partial_x E_z - i\omega\mu_0\left\{\sigma_{xx}E_x + \sigma_{xy}E_y + \sigma_{xz}E_z\right\} = i\omega\mu_0 J_x, \quad (3)$$

$$\partial_z\partial_y E_z - \partial_z^2 E_y - \partial_x^2 E_y + \partial_x\partial_y E_x - i\omega\mu_0\left\{\sigma_{yx}E_x + \sigma_{yy}E_y + \sigma_{yz}E_z\right\} = i\omega\mu_0 J_y, \quad (4)$$

$$\partial_x\partial_z E_x - \partial_x^2 E_z - \partial_y^2 E_z + \partial_y\partial_z E_y - i\omega\mu_0\left\{\sigma_{zx}E_x + \sigma_{zy}E_y + \sigma_{zz}E_z\right\} = i\omega\mu_0 J_z, \quad (5)$$

in a global x-y-z coordinate system that does not necessarily coincide with the principal-axis coordinate system of the medium.

PDEs (3)–(5) form the basis for our anisotropic frequency-domain CSEM modelling. The boundaries of the computational domain are assumed to be located sufficiently far away from the transmitter for the EM fields to have negligible values. Hence, we apply homogeneous Dirichlet boundary conditions by setting the EM field values to zero at the outermost boundaries of the FD mesh.

Lebedev grid discretization and system matrix

The unknown fields **E** and **H** are determined by the method of FDs on a Lebedev grid (Lebedev 1964). In this grid, all components of the electric field are collocated, but half a spatial step staggered by the collocated magnetic field components. To construct a Lebedev grid, we consider a tensor-product Cartesian grid defined by a set of N_x, N_y and N_z cells, respectively, in the x-, y- and z-directions. Let an indicial notation $(x_{i'}, y_{j'}, z_{k'})$ represent a point $\mathbf{r} \equiv x_{i'}\hat{\mathbf{x}} + y_{j'}\hat{\mathbf{y}} + z_{k'}\hat{\mathbf{z}}$ on this Cartesian grid, where the primed-subscripts take both integer (i.e. 1, 2, ...) and half-integer (i.e. $1 + 1/2$, $2 + 1/2$, ...) values. We assign all components of **E** to nodes for which $i' + j' + k'$ is half-integer and all components of **H** to nodes where the sum is integer. Consider a cell with top left corner node (x_i, y_j, z_k) where all subscripts are integer, then all components of **E** are located at $(x_{i+1/2}, y_j, z_k)$, $(x_i, y_{j+1/2}, z_k)$, $(x_i, y_j, z_{k+1/2})$ and $(x_{i+1/2}, y_{j+1/2}, z_{k+1/2})$. Here, $x_{i+1/2}$ represents $x_i + \triangle x_i/2$ and so on, where $\triangle x_i$, $\triangle y_j$ and $\triangle z_k$ are the dimensions of the grid cell (i, j, k), respectively, in the x-, y- and z-directions. In the same cell, all components of **H** are located at (x_i, y_j, z_k), $(x_i, y_{j+1/2}, z_{k+1/2})$, $(x_{i+1/2}, y_j, z_{k+1/2})$ and $(x_{i+1/2}, y_{j+1/2}, z_k)$. Fig. 1(a) shows the **E** and **H** fields locations on the Lebedev grid. Similar to the Yee grid, **E** and **H** are staggered by half a spatial step.

As described by Davydycheva *et al.* (2003) and Nauta *et al.* (2013), a Lebedev grid can be thought of as a superposition of four shifted Yee grids; for example those shown in Figs 1(b)–(e). To demonstrate this, we consider the standard Yee grid (Fig. 1b) where the **E** and **H** components have the indices

$$E_x(x_{i+1/2}, y_j, z_k),\ E_y(x_i, y_{j+1/2}, z_k),\ E_z(x_i, y_j, z_{k+1/2}),$$

$$H_x(x_i, y_{j+1/2}, z_{k+1/2}),\quad H_y(x_{i+1/2}, y_j, z_{k+1/2}),\quad H_z(x_{i+1/2}, y_{j+1/2}, z_k).$$

We call this Yee grid as subgrid 1, or cluster 000 as in Davydycheva *et al.* (2003). Let us consider a grid constructed from the standard Yee grid by shifting the components of **E** and **H** by $\triangle x_i/2$ and $\triangle y_j/2$, respectively, in the $(+/-)$ x- and $(+/-)$ y-directions (Fig. 1c). On this shifted Yee grid, the components of **E** and **H** have the indices

$$E_x(x_i, y_{j+1/2}, z_k),\ E_y(x_{i+1/2}, y_j, z_k),\ E_z(x_{i+1/2}, y_{j+1/2}, z_{k+1/2}),$$

$$H_x(x_{i+1/2}, y_j, z_{k+1/2}),\ H_y(x_i, y_{j+1/2}, z_{k+1/2}),\ H_z(x_i, y_j, z_k).$$

This grid is referred to as subgrid 2 or cluster 110. Similarly, subgrid 3 (or cluster 101) is constructed by shifting the components of **E** and **H** by $\triangle x_i/2$ and $\triangle z_k/2$, respectively, in the $(+/-)$ x- and $(+/-)$ z-directions (Fig. 1d), and subgrid 4 (or cluster 011) by $\triangle y_j/2$ and $\triangle z_k/2$, respectively, in the $(+/-)$ y- and $(+/-)$ z-directions (Fig. 1e). Subgrids 3 and 4 are defined by, respectively,

$$E_x(x_i, y_j, z_{k+1/2}),\ E_y(x_{i+1/2}, y_{j+1/2}, z_{k+1/2}),\ E_z(x_{i+1/2}, y_j, z_k),$$

$$H_x(x_{i+1/2}, y_{j+1/2}, z_k),\ H_y(x_i, y_j, z_k),\ H_z(x_i, y_{j+1/2}, z_{k+1/2}),$$

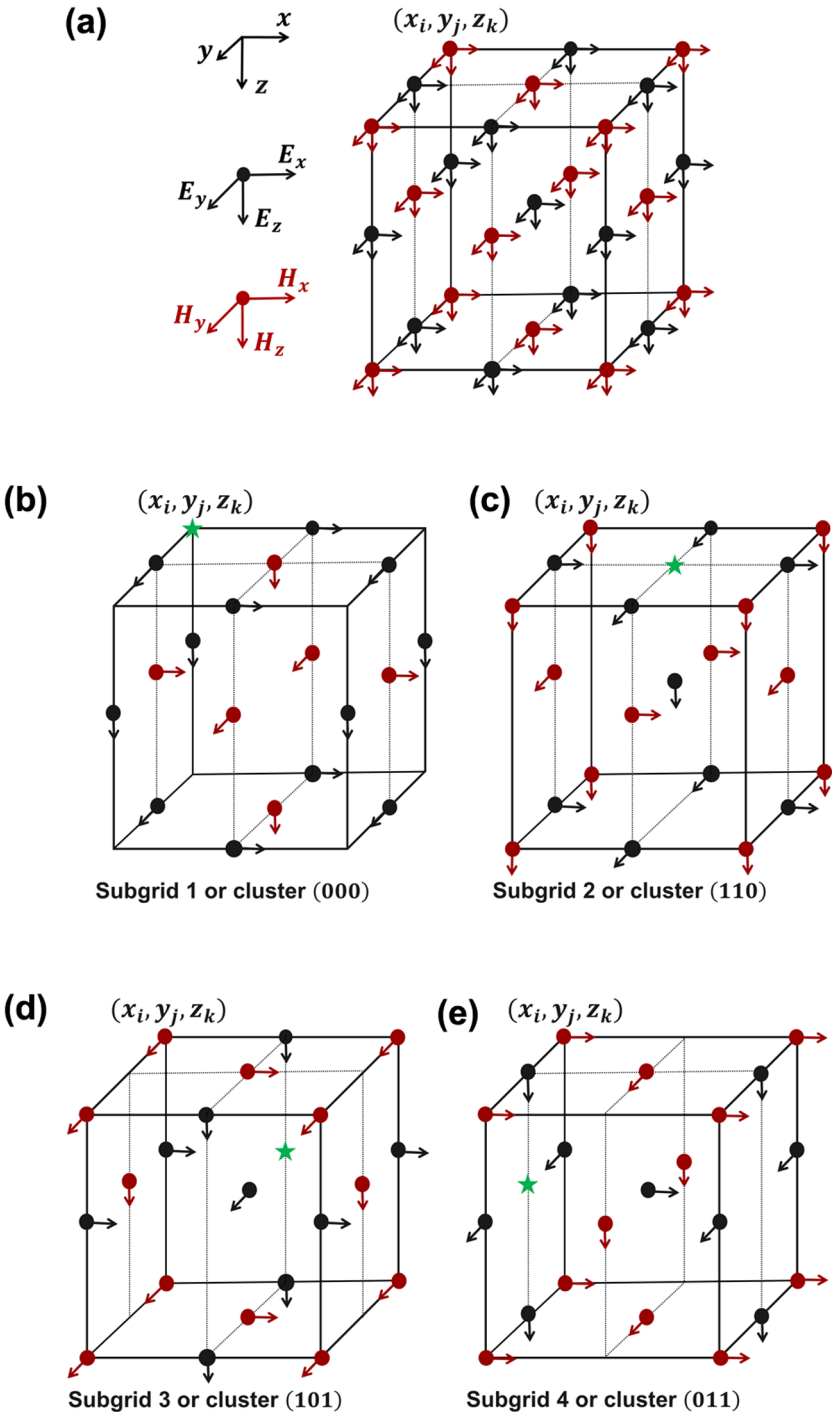

Figure 1. (a) Lebedev grid cell used to define the collocated electric and magnetic field components. (b) Standard Yee grid, and (c, d and e) the complementary Yee grids constructed by shifting the components of **E** and **H** by half a cell in the x-, y- and z-directions as explained in the text.

and

$$E_x(x_{i+1/2}, y_{j+1/2}, z_{k+1/2}),\ E_y(x_i, y_j, z_{k+1/2}),\ E_z(x_i, y_{j+1/2}, z_k),$$

$$H_x(x_i,\ y_j,\ z_k),\ H_y(x_{i+1/2},\ y_{j+1/2},\ z_k),\ H_z(x_{i+1/2},\ y_j,\ z_{k+1/2}).$$

Superposition of these four shifted Yee grids results in the Lebedev grid shown in Fig. 1(a). For anisotropic media, these subgrids are coupled since the off-diagonal elements of the conductivity tensor are non-zero, and hence the current density term in eq. (3), that is $(\tilde{\boldsymbol{\sigma}}\mathbf{E})_x = \sigma_{xx}\ E_x + \sigma_{xy}E_y + \sigma_{xz}E_z$, requires knowledge not only of E_x at a given node, but also of E_y and E_z at the same node, which belong to different subgrids. Similarly, the current density term in eqs (4) and (5) requires knowledge of **E** components belonging to different subgrids at the same node. However, if the conductivity tensor is diagonal (isotropic, VTI, HTI, or triaxial anisotropic medium), eqs (3)–(5) imply that on each subgrid, computation of the current density term requires only one component of **E** from the same subgrid. In other words, these subgrids are decoupled for a diagonal conductivity tensor.

Fig. 1 indicates that the FD discretization of eqs (3)–(5) requires conductivity values at electric field nodes (cell centre and halfway along cell edges). A constant conductivity is assumed within each cell, but it usually varies from cell to cell. This implies that the conductivity at the cell edges could be discontinuous, and hence a proper conductivity averaging is required. We follow a homogenization formula described in Davydycheva *et al*. (2003) to compute averaged conductivity at the nodes.

The discrete FD approximations of eqs (3)–(5) on a Lebedev grid can easily be obtained by combining the discrete FD approximations on the above four Yee grids. One can follow the FD approximations of derivatives in the PDEs (3)–(5) on the standard Yee grid given by Newman & Alumbaugh (1995) and extend them to the remaining shifted Yee grids. For example, the FD approximations of $\partial_y^2 E_x$ and $\partial_y \partial_x E_y$ at $(x_i,\ y_{j+1/2},\ z_k)$ on subgrid 2 are

$$\left.\frac{\partial^2 E_x}{\partial y^2}\right|_{i,j+\frac{1}{2},k} \approx \frac{1}{\triangle y_{sj}\triangle y_{sj+1}}\left[\frac{\triangle y_{sj}}{\triangle y_j}E^x_{i,j+\frac{3}{2},k} - \frac{(\triangle y_{sj}+\triangle y_{sj+1})}{\triangle y_j}E^x_{i,j+\frac{1}{2},k} + \frac{\triangle y_{sj+1}}{\triangle y_j}E^x_{i,j-\frac{1}{2},k}\right], \quad (6)$$

$$\left.\frac{\partial^2 E_y}{\partial y \partial x}\right|_{i,j+\frac{1}{2},k} \approx \frac{1}{\triangle x_{si}\triangle y_j}\left[E^y_{i+\frac{1}{2},j+1,k} - E^y_{i+\frac{1}{2},j,k} - E^y_{i-\frac{1}{2},j+1,k} + E^y_{i-\frac{1}{2},j,k}\right], \quad (7)$$

where $\triangle y_{sj} = \frac{1}{2}(\triangle y_{j-1} + \triangle y_j)$ and so on. Similarly, we can compute the FD approximations for all derivatives in the PDEs (3)–(5) on all shifted Yee grids.

The FD discretization of eqs (3)–(5) on a Lebedev grid results in a system of linear equations

$$\mathbf{Mx} = \mathbf{s}, \quad (8)$$

where $\mathbf{M}$ is the system matrix of dimension $12N \times 12N$ for a modelling grid with $N = N_x \times N_y \times N_z$ cells, $\mathbf{x}$ is a vector of dimension $12N$ containing unknown electric field components E_x, E_y and E_z, and $\mathbf{s}$ (dimension $12N$) is the source vector resulting from the right hand side of eq. (1). The matrix $\mathbf{M}$ is a sparse, complex and non-Hermitian matrix, having up to 15 non-zero elements in a row.

Iterative solver and preconditioning

The matrix eq. (8) is solved using a preconditioned BiCGStab(2) (van der Vorst 1992; Gutknecht 1993) algorithm, which is a Krylov subspace method. A preconditioner is crucial specifically for poorly conditioned matrices to accelerate the convergence of Krylov subspace solvers. The poor conditioning of a system matrix may be caused due to presence of a highly resistive air layer, which gives a large null-space to the 3-D curl–curl operator, and/or large cell aspect ratios, for example in the air layer and thick boundary paddings.

Preconditioning transforms the original linear system (8) into a preconditioned system, which has a smaller condition number than the original one (Saad 2003). For a preconditioning matrix $\mathbf{P}$, eq. (8) can be written into its left preconditioned form as

$$\mathbf{P}^{-1}\mathbf{Mx} = \mathbf{P}^{-1}\mathbf{s}, \quad (9)$$

which gives the same solution as the original matrix eq. (8). The preconditioning matrix $\mathbf{P}$ should be chosen such that $\mathbf{P}^{-1}\mathbf{M}$ is as close to the identity matrix as possible. In this work a multigrid preconditioner $\mathbf{P}$ is used. In other words, whenever we need to compute a product $\mathbf{P}^{-1}$ by some vector $\boldsymbol{z}$ and assign it to vector $\boldsymbol{y}$ (i.e. to find $\mathbf{y} = \mathbf{P}^{-1}\mathbf{z}$), we use a multigrid solver to find an approximate solution of the linear system $\mathbf{M}\boldsymbol{y} = \boldsymbol{z}$. On every BiCGStab iteration, one needs to compute product of $\mathbf{P}^{-1}$ by a vector two times: on steps 4 and 7 on the BiCGStab algorithm (see Algorithm 1). In computations, we used BiCGStab(2) method which is slightly more advanced than BiCGStab presented in Algorithm 1, but it also requires solution of the same two linear systems in each iteration.

Algorithm 1. Preconditioned BiCGStab algorithm with a preconditioning matrix $\mathbf{P}$.

1. Compute the initial residual: $\mathbf{r}_0 = \mathbf{s} - \mathbf{Mx}_0$ for an initial guess $\mathbf{x}_0$
2. Select an arbitrary vector $\tilde{\mathbf{r}}_0$ such that the inner product $(\mathbf{r}_0, \tilde{\mathbf{r}}_0) \neq 0$, e.g. $\tilde{\mathbf{r}}_0 = \mathbf{r}_0$
3. Set the initial search direction $\mathbf{a}_0 = \mathbf{r}_0$
   for $i = 0, 1, 2, \ldots$ *until convergence* **do**:
4. $\hat{\mathbf{a}}_i = \mathbf{P}^{-1}\,\mathbf{a}_i$
5. $\alpha_i = (\mathbf{r}_i, \tilde{\mathbf{r}}_0)/(\mathbf{M}\hat{\mathbf{a}}_i, \tilde{\mathbf{r}}_0)$
6. $\mathbf{b}_i = \mathbf{r}_i - \alpha_i \mathbf{M}\hat{\mathbf{a}}_i$
7. $\hat{\mathbf{b}}_i = \mathbf{P}^{-1}\,\mathbf{b}_i$
8. $\omega_i = (\mathbf{b}_i, \mathbf{M}\hat{\mathbf{b}}_i)/(\mathbf{M}\hat{\mathbf{b}}_i, \mathbf{M}\hat{\mathbf{b}}_i)$
9. $\mathbf{x}_{i+1} = \mathbf{x}_i + \alpha_i \hat{\mathbf{a}}_i + \omega_i \hat{\mathbf{b}}_i$
10. $\mathbf{r}_{i+1} = \mathbf{b}_i - \omega_i \mathbf{M}\hat{\mathbf{b}}_i$
11. $\beta_i = \alpha_i(\mathbf{r}_{i+1}, \tilde{\mathbf{r}}_0)/\omega_i\,(\mathbf{r}_i, \tilde{\mathbf{r}}_0)$
12. $\mathbf{a}_{i+1} = \mathbf{r}_i + \beta_i(\mathbf{a}_i - \omega_i \mathbf{M}\hat{\mathbf{a}}_i)$
    end

MULTIGRID METHOD

The multigrid method provides a means to iteratively solve systems of equations arising from the discretisation of elliptic boundary value problems. It is built on two basic principles (Wesseling 1991; Briggs *et al*. 2000; Trottenberg *et al*. 2001).

First, many classical iterative methods (e.g. Jacobi, Gauss-Seidel, etc.) have a strong error smoothing effect which makes them very effective at eliminating the oscillatory or high-frequency components of the error in a few iterations only, while leaving the smooth or low-frequency components relatively unchanged. The slow convergence of the classical iterative methods is mainly due to the slower elimination of the smooth components. These classical iterative methods are also referred to as smoothers or relaxation methods.

The second principle is the coarse-grid principle, which implies that a smooth error term on a finer grid can be accurately represented on a coarser grid essentially without any loss of information. Moreover, the smooth error components on the fine grid become more oscillatory on the coarse grid.

These two principles suggest that a coarse grid can be used to eliminate the smooth error components quickly. For this, we first relax the linear system on the fine grid using a smoother. After a few iterations of the smoother (usually 1, 2 or 3), relaxation begins to stall, indicating the dominance of smooth error components on this grid. We then move to a coarser grid, where the smooth error components appear more oscillatory, and hence the smoother eliminates them more efficiently. These are the main ideas of the so-called coarse-grid correction scheme. In a multigrid method, this scheme is applied recursively.

The multigrid method can be used as a standalone solver or as a preconditioner for another solver, for example BiCGStab. In both

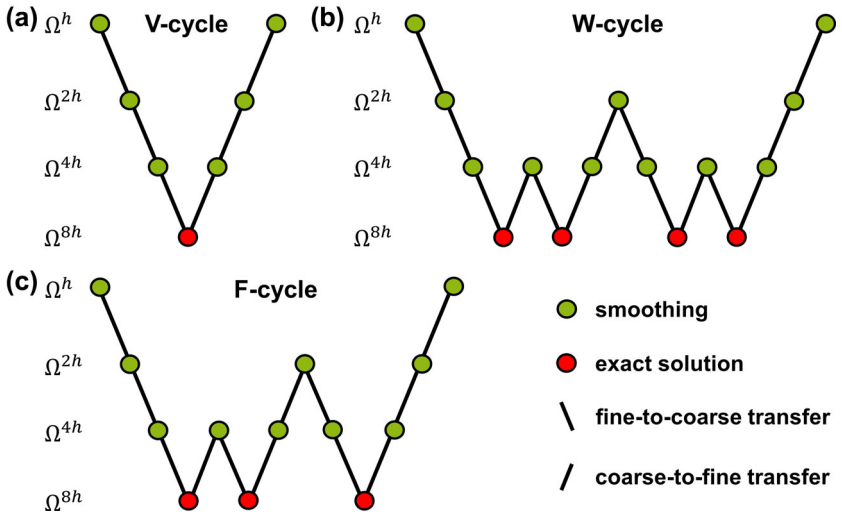

Figure 2. Structure of one multigrid cycle: (a) V-cycle, (b) W-cycle and (c) F-cycle. The finest grid has a cell-size of h and the coarsest $8h$.

cases, one looks for an approximate solution of a linear system of the type

$$\mathbf{M}\mathbf{y} = \mathbf{z}. \tag{10}$$

If the multigrid solver is used as a preconditioner for BiCGStab, this system needs to be solved on steps 4 and 7 of the BiCGStab method (Algorithm 1), where $\mathbf{z}$ is a known vector ($\mathbf{a}_i$ or $\mathbf{b}_i$) and $\mathbf{y}$ is an unknown vector ($\hat{\mathbf{a}}_i$ or $\hat{\mathbf{b}}_i$). Note that the inverse preconditioning matrix $\mathbf{P}^{-1}$ appearing in the Algorithm 1 is never computed explicitly: it is only implicitly defined by the equation $\tilde{\mathbf{y}} = \mathbf{P}^{-1}\, z$, where $\tilde{\mathbf{y}}$ is an approximate solution of eq. (10) obtained by the full multigrid cycle.

If we denote the matrix $\mathbf{M}$ as $\mathbf{M}^h$ and the vectors $\mathbf{y}$ and $\mathbf{z}$ as $\mathbf{y}^h$ and $\mathbf{z}^h$ on a modelling grid Ω^h with cell size h then eq. (10) reads

$$\mathbf{M}^h\, \mathbf{y}^h = \mathbf{z}^h. \tag{11}$$

For the coarse-grid correction, first a smoother or relaxation operator $S^h(\mathbf{M}^h,\ \mathbf{z}^h,\ \mathbf{y}_0^h)$ is applied to compute an approximation $\tilde{\mathbf{y}}^h$ of $\mathbf{y}^h$ as

$$\tilde{\mathbf{y}}^h = S^h\ \left(\mathbf{M}^h,\ \mathbf{z}^h,\ \mathbf{y}_0^h\right), \tag{12}$$

where $\mathbf{y}_0^h$ is an initial guess. The vector $\tilde{\mathbf{y}}^h$ approximates the oscillatory part of the solution well after a few pre-smoothing iterations, say n_1. The error in this approximation is $\mathbf{e}^h = \mathbf{y}^h - \tilde{\mathbf{y}}^h$, which satisfies the following residual equation of the linear eq. (11)

$$\mathbf{M}^h\ \mathbf{e}^h = \mathbf{r}^h, \tag{13}$$

where $\mathbf{r}^h = \mathbf{z}^h - \mathbf{M}^h\ \tilde{\mathbf{y}}^h$ is the residual. At this point, the residual $\mathbf{r}^h$ is transferred to a coarser grid Ω^{2h} with the cell size $2h$. This is achieved using a restriction operator I_h^{2h} such that $\mathbf{r}^{2h} = I_h^{2h}\ \mathbf{r}^h$ on Ω^{2h}. Therefore, the residual equation becomes

$$\mathbf{M}^{2h}\ \ \mathbf{e}^{2h} = \mathbf{r}^{2h} \tag{14}$$

on Ω^{2h}. This problem (eq. 14) can be solved for $\mathbf{e}^{2h}$ using a direct solver if the number of unknowns on the coarser grid Ω^{2h} is sufficiently small. The computed error $\mathbf{e}^{2h}$ (or the coarse-grid correction) on Ω^{2h} then needs to be transferred back to the modelling grid Ω^h. This is achieved using an interpolation or prolongation operator I_{2h}^h such that $\mathbf{e}^h = I_{2h}^h\ \mathbf{e}^{2h}$. The fine-grid error is then used to update the approximate solution $\tilde{\mathbf{y}}^h$, obtained after n_1 pre-smoothing iterations, as $\tilde{\mathbf{y}}^h := \tilde{\mathbf{y}}^h + \mathbf{e}^h$. Finally, n_2 additional smoothing iterations (post-smoothing iterations) are applied on the fine-grid. This constitutes one iteration of the coarse-grid correction.

If the number of unknowns on the coarse grid Ω^{2h} is too large to be handled by a direct solver, we apply the above procedure recursively by considering successive coarser grids, for example Ω^{2h}, Ω^{4h}, $\Omega^{8h}\ldots\ \Omega^{Lh}$, respectively, with the cell sizes $2h$, $4h$, $8h, \ldots\ Lh$, where $L = 2^l$ for $l \geq 1$.

The multigrid method can visit the coarser grids in different ways, as illustrated in Fig. 2 presenting the three main types of multigrid cycles (Briggs *et al.* 2000): V-, W- and F-cycles. The simplest one is the V-cycle, in which the coarse-grid correction scheme is recursively applied only once at each successive multigrid level, while in the most powerful W-cycle it is applied twice. The F-cycle is a good compromise: its convergence is faster than for the cheap V-cycle, but only slightly slower than for the expensive W-cycle.

For all the modelling examples, we chose the F-cycle with two post-smoothing iterations ($n_2 = 2$), while the number of pre-smoothing iterations is zero ($n_1 = 0$). In the following, we describe our selection of the smoother, prolongation, restriction and coarse-grid operators in detail.

Smoother or relaxation

In our implementation, we follow the method introduced by Arnold *et al.* (2000) to choose a smoother. For the Yee grid, Mulder (2006) implemented this method as a smoother for the linear system obtained using the FI discretization of Maxwell's equations. It selects one node of a cell and simultaneously solves a local 6×6 linear system for six unknowns on the six edges attached to the node. If node $(x_i,\ y_j,\ z_k)$ is selected, the six equations are solved for unknowns $F^x_{i\pm1/2,j,k}$, $F^y_{i,j\pm1/2,k}$ and $F^z_{i,j,k\pm1/2}$. Here, the unknowns F_x, F_y and F_z are part of the vector $\mathbf{y}$ in eq. (10) and their values at node $(x_{i\pm1/2},\ y_j,\ z_k)$ are indexed as $F^x_{i\pm1/2,j,k} \equiv F_x(x_{i\pm1/2},\ y_j,\ z_k)$, and so on.

This smoother follows the lexicographical ordering of the cells (i, j, k), with the fastest index $i = 1, \ldots, N_x$, intermediate index $j = 1, \ldots, N_y$ and the slowest index $k = 1, \ldots, N_z$. In addition, it is applied in a symmetric Gauss–Seidel fashion. The first smoothing iteration follows this lexicographical ordering and solves for $F^x_{i\pm1/2,j,k}$, $F^y_{i,j\pm1/2,k}$ and $F^z_{i,j,k\pm1/2}$ at all the selected nodes on the FD grid, and hence gives an approximation of $\mathbf{y}$. The next smoothing

iteration is performed in the opposite direction, that is fastest index $i = N_x, \ldots, 1$, intermediate index $j = N_y, \ldots, 1$ and the slowest index $k = N_z, \ldots, 1$; this smoothing iteration updates the values of $F^x_{i\pm1/2,j,k}$, $F^y_{i,j\pm1/2,k}$ and $F^z_{i,j,k\pm1/2}$ (i.e. the approximate values of $\mathbf{y}$), computed during the previous lexicographical-ordered smoothing iteration. Therefore, one iteration of the smoother in the symmetric Gauss–Seidel fashion is equivalent to two smoothing iterations, that is n_1 or $n_2 = 2$. This smoother has an important property that it locally imposes the divergence-free characteristics of the current density, that is $\nabla.\bar{\sigma}\mathbf{E} = 0$, each time a 6×6 matrix is solved at a selected node (Mulder 2006). Even though this property is lost from one node to another, this provides sufficient damping to the large null-space of the 3-D curl-curl operator to avoid convergence issues. Therefore, an explicit divergence correction (Smith 1996) is not required.

We extend this smoothing method for the FD discretization of Maxwell's equation on the Lebedev grid, where it selects four nodes in each cell and solves four local 6×6 linear systems for unknowns adjacent to each of the four selected nodes. These four nodes include one corner node $(x_i,\ y_j,\ z_k)$ and three face-centred nodes defined at $(x_{i+1/2},\ y_{j+1/2},\ z_k)$, $(x_{i+1/2},\ y_j,\ z_{k+1/2})$ and $(x_i,\ y_{j+1/2},\ z_{k+1/2})$. The unknowns are located at half a cell size away from each of these nodes in the $\pm x$-, $\pm y$- and $\pm z$-directions. Therefore, if the smoother selects node $(x_i,\ y_j,\ z_k)$ (star in Fig. 1b), the six equations are solved for unknowns $F^x_{i\pm1/2,j,k}$, $F^y_{i,j\pm1/2,k}$ and $F^z_{i,j,k\pm1/2}$. For node $(x_{i+1/2},\ y_{j+1/2},\ z_k)$ (star in Fig. 1c), the six equations are solved for unknowns $F^x_{i+1/2\pm1/2,j+1/2,k}$, $F^y_{i+1/2,j+1/2\pm1/2,k}$ and $F^z_{i+1/2,j+1/2,k\pm1/2}$. For node $(x_{i+1/2},\ y_j,\ z_{k+1/2})$ (star in Fig. 1d), the six equations are solved for unknowns $F^x_{i+1/2\pm1/2,j,k+1/2}$, $F^y_{i+1/2,j\pm1/2,k+1/2}$ and $F^z_{i+1/2,j,k+1/2\pm1/2}$. Finally, for node $(x_i,\ y_{j+1/2},\ z_{k+1/2})$ (star in Fig. 1e), the six equations are solved for unknowns $F^x_{i\pm1/2,j+1/2,k+1/2}$, $F^y_{i,j+1/2\pm1/2,k+1/2}$ and $F^z_{i,j+1/2,k+1/2\pm1/2}$.

Prolongation, restriction and coarse-grid operators

We assume that $N_x = 2^{n_x} p$, $N_y = 2^{n_y} q$ and $N_z = 2^{n_z} r$ with integers $n_x \geq 1, n_y \geq 1$ and $n_z \geq 1$, and p, q and $r = 1, 3$, or 5. This choice assures an easy construction of the coarse-grid Ω^{2h} by selecting every other point of x^h_i $(i = 1, 2, \ldots N_x)$, y^h_j $(j = 1, 2, \ldots N_y)$ and z^h_k $(k = 1, 2, \ldots N_z)$ of the fine grid Ω^h. Hence, the main nodes of the coarse grid become $(x^{2h}_I,\ y^{2h}_J,\ z^{2h}_K)$ with $I = (i+1)/2$, $J = (j+1)/2$ and $K = (k+1)/2$ for $i = 1,\ 3, \ldots N_x - 1$, $j = 1,\ 3, \ldots N_y - 1$ and $k = 1,\ 3, \ldots N_z - 1$. Fig. 3 illustrates a coarse grid cell obtained by combining eight fine grid cells (blue), that is two fine grid cells in each direction.

A prolongation operator I^h_{2h} is required to transfer the coarse-grid correction $\mathbf{e}^{2h}$ from the coarse grid Ω^{2h} to the fine grid Ω^h. We use constant, linear, bilinear and trilinear interpolations for this purpose depending on the node positions. For example, for the x-staggered nodes for $i_2 = 0,\ 1$, $j_2 = -1,\ 0,\ 1$ and $k_2 = -1,\ 0,\ 1$

$$e^h_{i+1/2+i_2,j+j_2,k+k_2} = w^y_{j_2}\, w^z_{k_2} e^{2h}_{I+1/2,J,K}, \tag{15}$$

where

$$w^y_{-1} = \frac{y^h_{j-1} - y^{2h}_{J-1}}{y^{2h}_J - y^{2h}_{J-1}},\quad w^y_0 = 1,\ \text{and}\ w^y_1 = \frac{y^{2h}_{J+1} - y^h_{j+1}}{y^{2h}_{J+1} - y^{2h}_J}, \tag{16}$$

and

$$w^z_{-1} = \frac{z^h_{k-1} - z^{2h}_{K-1}}{z^{2h}_K - z^{2h}_{K-1}},\quad w^z_0 = 1,\ \text{and}\ w^z_1 = \frac{z^{2h}_{K+1} - z^h_{k+1}}{z^{2h}_{K+1} - z^{2h}_K}. \tag{17}$$

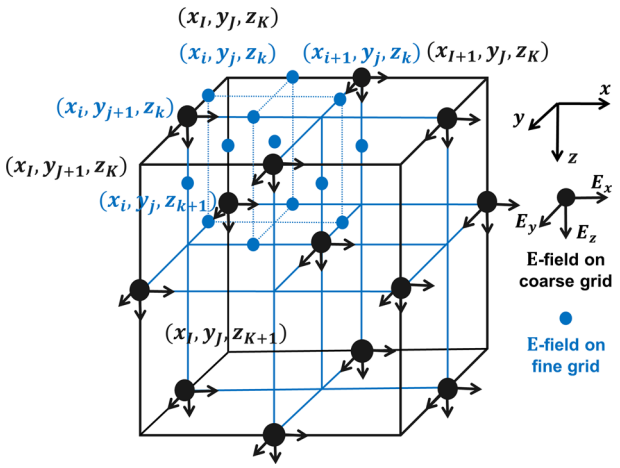

Figure 3. A coarse grid cell (black) obtained by combining eight fine grid cells (blue), that is two fine grid cells in each direction. Top-left corner node of a cell is denoted by $(x_i,\ y_j,\ z_k)$ on the fine grid and by $(x_I,\ y_J,\ z_K)$ on the coarse grid, where $I = (i+1)/2$, $J = (j+1)/2$, and $K = (k+1)/2$ for $i = 1,\ 3, \ldots N_x - 1$, $j = 1,\ 3, \ldots N_y - 1$, and $k = 1,\ 3, \ldots N_z - 1$.

Similarly, for the y-staggered node for $i_2 = -1,\ 0,\ 1$, $j_2 = 0,\ 1$ and $k_2 = -1,\ 0,\ 1$

$$e^h_{i+i_2,j+1/2+j_2,k+k_2} = w^x_{i_2}\, w^z_{k_2} e^{2h}_{I,J+1/2,K}, \tag{18}$$

and the z-staggered node for $i_2 = -1,\ 0,\ 1$, $j_2 = -1,\ 0,\ 1$ and $k_2 = 0,\ 1$

$$e^h_{i+i_2,j+j_2,k+1/2+k_2} = w^x_{i_2}\, w^y_{j_2} e^{2h}_{I,J,K+1/2}, \tag{19}$$

where

$$w^x_{-1} = \frac{x^h_{i-1} - x^{2h}_{I-1}}{x^{2h}_I - x^{2h}_{I-1}},\quad w^x_0 = 1,\ \text{and}\ w^x_1 = \frac{x^{2h}_{I+1} - x^h_{i+1}}{x^{2h}_{I+1} - x^{2h}_I}, \tag{20}$$

and $w^y_{j_2}$ for $j_2 = -1,\ 0,\ 1$ and $w^z_{k_2}$ for $k_2 = -1,\ 0,\ 1$ are, respectively, given in eqs (16) and (17).

For the cell-centred nodes defined at $(x_{i+1/2},\ y_{j+1/2},\ z_{k+1/2})$, we use a trilinear interpolation using

$$e^h_{i+1/2+i_2,j+1/2+j_2,k+1/2+k_2} = v^x_{i_2}\, v^y_{j_2} v^z_{k_2} e^{2h}_{I+1/2,J+1/2,K+1/2}, \tag{21}$$

for $i_2 = -1,\ 0,\ 1,\ 2$, $j_2 = -1,\ 0,\ 1,\ 2$ and $k_2 = -1,\ 0,\ 1,\ 2$. Here, the weights are

$$v^x_{-1} = \frac{x^h_{i-1/2} - x^{2h}_{I-1/2}}{x^{2h}_{I+1/2} - x^{2h}_{I-1/2}},\quad v^x_0 = \frac{x^h_{i+1/2} - x^{2h}_{I-1/2}}{x^{2h}_{I+1/2} - x^{2h}_{I-1/2}},$$

$$v^x_1 = \frac{x^{2h}_{I+3/2} - x^h_{i+3/2}}{x^{2h}_{I+3/2} - x^{2h}_{I+1/2}},\ \text{and}\ v^x_2 = \frac{x^{2h}_{I+3/2} - x^h_{i+5/2}}{x^{2h}_{I+3/2} - x^{2h}_{I+1/2}}. \tag{22}$$

Similarly, we define the weights $v^y_{j_2}$ and $v^z_{k_2}$, respectively, for $j_2 = -1,\ 0,\ 1,\ 2$ and $k_2 = -1,\ 0,\ 1,\ 2$.

For the cell-centred nodes, we have also experimented with a prolongation operator that is obtained by extending Mulder's (2006) implementation. The expression of this operator is the same as the expression given in eq. (21), but the weights and subscripts i_2, j_2 and k_2 are different: $v^x_{i_2} = v^y_{j_2} = v^z_{k_2} = 1$, and $i_2 = 0, 1$, $j_2 = 0, 1$ and $k_2 = 0, 1$. This operator is essentially a constant interpolation operator. However, we observed a slower convergence of the preconditioned solver with this operator than with our trilinear interpolation operator of eq. (21). Therefore, we have used the trilinear interpolation operator for all the modelling examples presented in this paper.

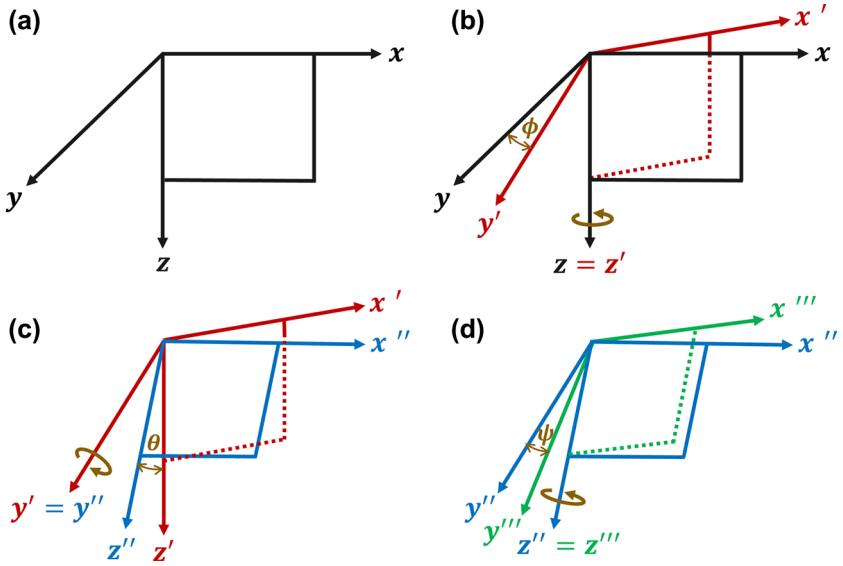

Figure 4. Illustration of successive Euler rotation of the global x-y-z coordinate system (a) to obtain any orientation of the anisotropic principal-axis coordinate system using anisotropic strike (ϕ), dip (θ) and slant (ψ) angles as shown in (b), (c) and (d), respectively.

A restriction operator I_h^{2h}, required to transfer the fine-grid residual $\mathbf{r}^h$ to the coarse-grid, is taken as the transpose of the prolongation operator I_{2h}^h. This implies that the same weights are used as in the prolongation operator. Therefore, for the x-, y- and z-staggered nodes, respectively,

$$r^{2h}_{I+1/2,J,K} = \sum_{j_2=-1}^{1}\sum_{k_2=-1}^{1} w^y_{j_2} w^z_{k_2} \left(r^h_{i+1/2,j+j_2,k+k_2} + r^h_{i+3/2,j+j_2,k+k_2}\right), \tag{23}$$

$$r^{2h}_{I,J+1/2,K} = \sum_{i_2=-1}^{1}\sum_{k_2=-1}^{1} w^x_{i_2} w^z_{k_2} \left(r^h_{i+i_2,j+1/2,k+k_2} + r^h_{i+i_2,j+3/2,k+k_2}\right), \tag{24}$$

and

$$r^{2h}_{I,J,K+1/2} = \sum_{i_2=-1}^{1}\sum_{j_2=-1}^{1} w^x_{i_2} w^y_{j_2} \left(r^h_{i+i_2,j+j_2,k+1/2} + r^h_{i+i_2,j+j_2,k+3/2}\right). \tag{25}$$

For the cell-centred node

$$r^{2h}_{I+1/2,J+1/2,K+1/2} = \sum_{i_2=-1}^{2}\sum_{j_2=-1}^{2}\sum_{k_2=-1}^{2} v^x_{i_2} v^y_{j_2} v^z_{k_2} r^h_{i+1/2+i_2,j+1/2+j_2,k+1/2+k_2}. \tag{26}$$

In the implementation, the coarse-grid operator $\mathbf{M}^{2h}$ is obtained using Galerkin coarse-grid approximation (Wesseling 1991). If $\mathbf{I}_h^{2h}$ is a restriction operator matrix of dimension $K \times N$ and $\mathbf{I}_{2h}^h$ is a prolongation operator matrix of dimension $N \times K$, then the coarse-grid operator is

$$\mathbf{M}^{2h} = \mathbf{I}_h^{2h}\, \mathbf{M}^h \mathbf{I}_{2h}^h. \tag{27}$$

The dimension of $\mathbf{M}^{2h}$ is $K \times K$, where $K = N/8$ for the coarse-grid Ω^{2h}. Note that $\mathbf{I}_{2h}^h = (\mathbf{I}_h^{2h})^{\mathrm{T}}$, where T represents the transpose operator. In practice, $\mathbf{I}_h^{2h}$ and $\mathbf{I}_{2h}^h$ are very sparse, and hence they lead to a very efficient computation of $\mathbf{M}^{2h}$.

BENCHMARKING RESULTS

In this section, we compare the simulation results produced by the developed multigrid preconditioner based 3-D anisotropic frequency-domain finite-difference (FDFD) modelling code against results produced by well-established methods.

For practical purposes, the electrical conductivity tensor of each model cell is described in a principal-axis coordinate system of the anisotropic medium. In this coordinate system, the anisotropic conductivity tensor $\bar{\boldsymbol{\sigma}}$ can be represented by a diagonal conductivity tensor $\bar{\boldsymbol{\sigma}}_D$ using elementary rotations by Euler angles ϕ, θ and ψ. These Euler angles ϕ, θ and ψ are, respectively, the anisotropic strike (rotation around z-axis in Fig. 4b), dip (rotation around y'-axis in Fig. 4c) and slant angles (rotation around z''-axis in Fig. 4d) (Martí 2014). These rotation angles can describe the orientation of the principal-axis coordinate system of any anisotropic medium. The anisotropic conductivity tensor $\bar{\boldsymbol{\sigma}}$ in the global x-y-z coordinate system can easily be recovered from the principal-axis coordinate system using a rotation matrix $\mathbf{R}$,

$$\bar{\boldsymbol{\sigma}} = \mathbf{R}^{\mathrm{T}}\, \bar{\boldsymbol{\sigma}}_D \mathbf{R}. \tag{28}$$

The elements of $\mathbf{R}$ are the sines and cosines of the angles between the principal-axis and global x-y-z coordinate systems. If the conductivity in the two of the three principal directions is equal (e.g. in a transverse isotropy), the elements of $\mathbf{R}$ can be uniquely expressed in terms of only two Euler angles corresponding to the strike ϕ and dip θ angles:

$$\mathbf{R} = \begin{bmatrix} \cos\theta\cos\phi & \cos\theta\sin\phi & -\sin\theta \\ -\sin\phi & \cos\phi & 0 \\ \sin\theta\cos\phi & \sin\theta\sin\phi & \cos\theta \end{bmatrix}. \tag{29}$$

For a TTI medium, $\bar{\boldsymbol{\sigma}}_D = \mathrm{diag}(\sigma_{x''}, \sigma_{y''}, \sigma_{z''})$, where $\sigma_{x''} = \sigma_{y''} := \sigma_T$(or $\rho_T{}^{-1}$) is the conductivity (or resistivity^{-1}) in the bed-parallel direction and $\sigma_{z''} := \sigma_N$(or $\rho_N{}^{-1}$) is the conductivity (or resistivity^{-1}) perpendicular to the bedding planes. Hence, the conductivity of each model cell can be specified with only four model parameters: σ_T, σ_N, ϕ and θ. For a VTI medium, the angles ϕ and θ are zero, and conductivities σ_T and σ_N are, respectively, the horizontal and vertical conductivities.

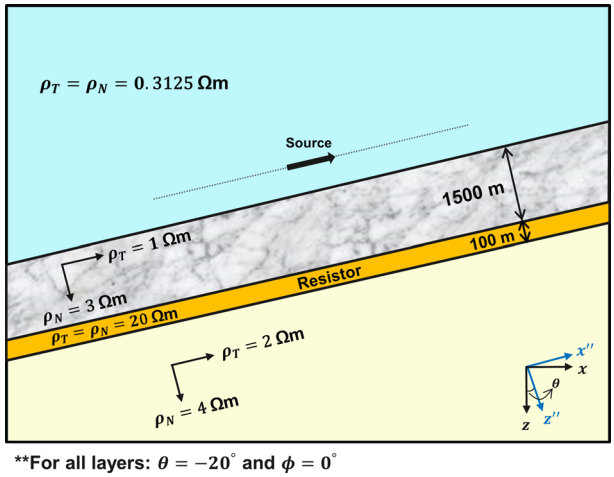

Figure 5. Vertical cross-section of a deep-water TTI layered earth model used for comparison with semi-analytical solutions.

Deep-water layered earth model

Let us consider the deep-water layered Earth resistivity model depicted in Fig. 5. The layers in the model are tilted with the dip angle $\theta = -20^\circ$, while the strike angle ϕ is zero. The anisotropic layers are assumed to be TTI ($\sigma_{x''} = \sigma_{y''}$) with their symmetry axis directed normal to the layers. The anisotropy factors (ρ_N/ρ_T) in different layers vary from one to three. The dimension of the model is $32 \times 25.6 \times 25.6$ km^3, which is sufficiently large for the EM fields to satisfy homogeneous Dirichlet conditions at the boundaries when the source is located in the central part of the model. The model was discretized with an FD grid having uniform cell sizes of 100 m in the x- and z-directions and 200 m in the y-direction. The FD discretization of the model resulted in $320 \times 128 \times 256$ cells, representing approximately 126 million degrees of freedom. The EM fields are excited by an x-oriented horizontal electric dipole (HED) source with frequencies 0.25 and 0.5 Hz towed 130 m above the tilted seabed.

We carried out all simulations sequentially on a computer with Intel Xeon CPU E5-2690 processors running at 2.90 GHz and 264 GB of memory. The resulting linear systems obtained using the FD discretization of the PDEs (3)–(5) were solved using the above-described multigrid preconditioned BiCGStab(2) solver. The iterations were stopped when the relative residual norm ($||\mathbf{Mx} - \mathbf{s}||/||\mathbf{s}||$) dropped below 10^{-8}. For 0.25 and 0.5 Hz frequencies, the solver, respectively, needed 11 and 9 iterations to solve the linear systems and the corresponding linear system solution time was 218 and 178 minutes.

We compare the 3-D simulation results obtained using the developed anisotropic FDFD method to reference fields calculated using a semi-analytical plane-layer method (Løseth & Ursin 2007). To compute semi-analytical results for this TTI model, we rotate the x-y-z coordinate system by the angle θ so that it coincides with the principal-axis coordinate system of the model—the same way as it was done in Shantsev & Maaø (2015). Fig. 6(a) shows the amplitude (left) and phase (right) responses for the x-component of the electric field (E_x) at 0.25 and 0.5 Hz along a receiver line located 100 m above the seabed. The horizontal electric field E_x is computed using electric field components, which are in the bed-parallel (the x''-component) and bed-perpendicular (the z''-component) directions. The solid lines and filled circles, respectively, show results obtained with our anisotropic 3-D FDFD method and the plane-layer method. The corresponding normalized amplitudes and phase differences between these results are shown in Fig. 6(b). Except for the responses that are very close to the source position, the field amplitudes differ at most by 2.1 and 2.0 per cent and the phases at most by 1.5 and 3°, respectively, for 0.25 and 0.5 Hz.

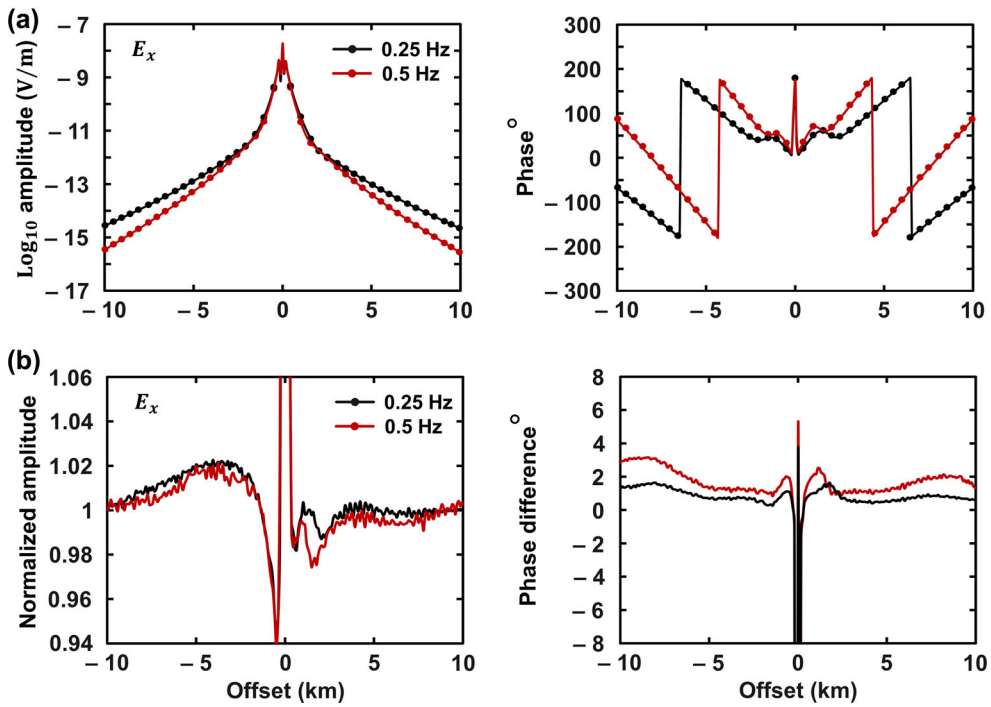

Figure 6. (a) Amplitude (left-hand panel) and phase (right-hand panel) responses of E_x at 0.25 and 0.5 Hz for the deep-water TTI model of Fig. 5. They are calculated using the developed anisotropic 3-D FDFD method (solid lines) and the plane-layer method of Løseth & Ursin (2007) (filled circles). (b) Normalized amplitude (left-hand panel) and phase difference (right-hand panel) between responses calculated using these two methods.

Table 1. Uniform discretizations of the deep-water layered earth TTI model and the corresponding runtime statistics for the linear system solution. Here in the x-, y- and z-directions, dx, dy and dz are the cell sizes, and N_x, N_y and N_z are the number of cells. $12N = 12N_xN_yN_z$ is the total number of unknowns, N_{iter} is the number of BiCGStab(2) iterations required for the relative residual norm to drop below 10^{-8}, and T is the linear system solution time.

							N_{iter}		T (s)	
dx	dy	dz	N_x	N_y	N_z	$12N$	$f = 0.25$ Hz	$f = 0.5$ Hz	$f = 0.25$ Hz	$f = 0.5$ Hz
100	200	100	320	128	256	125 829 120	11	9	13 121.4	10 685.1
200	200	100	160	128	256	62 914 560	10	8	6130.0	4809.6
200	200	200	160	128	128	31 457 280	8	7	2059.7	1765.2
400	400	200	80	64	128	7864 320	6	4	427.6	282.3
400	400	400	80	64	64	3932 160	4	4	135.2	132.4
800	800	800	40	32	32	491 520	4	4	16.8	16.7

We also computed relative errors,

$$\sqrt{\frac{|E^{\text{true}} - E^{\text{FD}}|^2}{|E^{\text{true}}|^2 + \eta^2}}, \tag{30}$$

averaged over source–receiver offsets from -10 to 10 km, where E^{true} and E^{FD} are the complex-valued electric fields computed using the plane-layer and anisotropic 3-D FDFD methods, respectively. The term η representing the ambient noise level is added to prevent unreasonably large relative errors when the field is close to zero. We also exclude offsets shorter than 1 km where the relative errors are very much affected by discretization errors due to fast variations of the fields in space. The average relative errors (with $\eta = 5 \times 10^{-17}$ Vm^{-1}) are 1.8 and 2.8 per cent, respectively, for 0.25 and 0.5 Hz frequencies. These errors imply that the developed anisotropic 3-D FDFD algorithm provides quite accurate results for the deep-water TTI layered earth model with 20-degree dip and anisotropy factors up to three. It is important to emphasize that we also expect some portion of the error due to the staircase approximation of the tilted interfaces in the FD discretization of the model. Note also that the modelled resistor is only one cell thick and in addition is tilted relative to the grid. Thus the observed small errors is quite an impressive result for a finite difference code, which to a large degree is due to an efficient cell homogenization scheme adopted from Davydycheva *et al*. (2003).

Let us now examine how performance of the multigrid preconditioned BiCGStab(2) solver depends on the system size. We carried out forward simulations on the same resistivity model, but with five different discretizations which resulted in different number of unknowns varying from ∼126 million to ∼0.5 million. The number of BiCGStab(2) iterations and the time spent to solve the linear systems for each case are given in Table 1. We notice that the solver needed somewhat more iterations for the bigger linear systems than for the smaller ones. Meanwhile, the solution time increased approximately linearly with the number of unknowns. A similar trend was observed for a BiCGStab solver with an algebraic multigrid preconditioner implemented for the FE discretization by Koldan *et al*. (2014).

Shallow-water layered earth model

Fig. 7 shows the shallow-water layered earth model with 200 m of seawater. The EM fields are excited by an x-oriented HED with a frequency of 0.5 Hz towed 30 m above the seabed. The dimension of the model is $20 \times 20 \times 6$ km^3. We shall refer to this domain as the 'domain of interest', which includes the source and receivers. For shallow-water models, it is essential to include a thick air layer above the sea surface; therefore, the top boundary of the computational domain included an air layer of thickness ∼ 50 km and resistivity

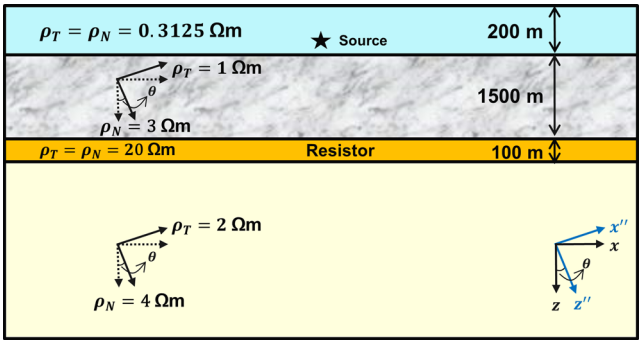

Figure 7. Vertical cross-section of a shallow-water layered earth model. The model also includes an air layer of thickness ∼50 km and resistivity 10^6 Ωm above the seawater. For a shallow-water VTI model, the anisotropic layers (above and below the isotropic reservoir) have zero dip and zero strike angles ($\theta = \phi = 0^\circ$), while for a TTI model, they are assumed to have tilted anisotropy with dip angle $\theta = -20^\circ$ and strike angle $\phi = 0^\circ$.

10^6 Ωm. In addition, 30 km padding was added at the vertical and bottom boundaries of the domain of interest along with the air layer to avoid edge effects due to the combination of strong shallow-water airwave and zero-field Dirichlet boundary conditions. This additional padding is referred to as the 'extended domain' and it has proven to be critical to ensure good modelling accuracy (Jaysaval *et al*. 2015).

In the previous deep-water layered Earth case, we validated the accuracy of the developed anisotropic 3-D FDFD results against semi-analytical solutions obtained using the plane-layer method developed by Løseth & Ursin (2007). This plane-layer method is only applicable for VTI layered earth models. To compute a semi-analytical solution for the deep-water TTI layered earth model with axis of symmetry normal to the tilted interfaces, we rotated the x-y-z coordinate system so that it coincides with the principal-axis coordinate system of the model. This simple approach, however, is not applicable for similar shallow-water TTI layered earth models because, otherwise, the air-water interface becomes a tilted interface, which cannot exist in the real world. Therefore, we first consider the shallow-water VTI layered model of Fig. 7 and compare the developed anisotropic 3-D FDFD simulation results against the semi-analytical solutions. We subsequently assume that the anisotropic layers in this model have tilted anisotropy and then compare the anisotropic 3-D FDFD simulation results against results computed using COMSOL Multiphysics software.

Non-uniform grids were used to discretize the computational domain (including the domain of interest, air layer and extended domain). Away from the source the cell size increased according to a power law $dh\,(n) = \min(dh_{\min} \times \lambda^{n-1}, dh_{\max})$ where $h = x, y,$ or z; $n = 1, 2, \ldots\ldots$ is a cell counter; $dh_{\min}$ is the minimum cell size; $dh_{\max}$ is the maximum cell size; and λ is a constant growth

Table 2. Non-uniform discretizations of the shallow-water layered earth model and the corresponding runtime statistics for the linear system solution. Here in the x-, y- and z-directions, respectively, λ_x, λ_y and λ_z are the constant growth factors, $dx_{\min}$, $dy_{\min}$ and $dz_{\min}$ are the minimum cell sizes, $dx_{\max}$, $dy_{\max}$ and $dz_{\max}$ are the maximum cell sizes. The other nomenclatures are the same as in Table 1. The domain of interest refers to the main computational volume, which includes the source and receivers; whilst the extended domain refers to the padding added at the model boundaries to reduce the errors due to truncation of the unbounded domain. In the extended domain, the minimum cell sizes are equal to the corresponding maximum cell sizes in the domain of interest, while the maximum cell size is 4000 m in all directions, and $\lambda_x = \lambda_y = \lambda_z = \lambda$.

Domain of interest						Extended domain							
$\lambda_x = \lambda_y$	$dx_{\min} = dy_{\min}$ (m)	$dx_{\max} = dy_{\max}$ (m)	λ_z	$dz_{\min}$ (m)	$dz_{\max}$ (m)	$N_x = N_y$	N_z	λ	$N_x = N_y$	N_z	$12N$	N_{iter}	T (s)
1.019	60	270	1.039	20	200	156	108	1.16	36	20	56 623 104	69	36 834.1
1.039	70	440	1.051	30	250	98	78	1.16	30	18	18 874 368	62	9777.4
1.065	80	680	1.058	42	360	70	65	1.24	26	15	8847 360	44	3442.8
1.073	100	780	1.079	42	450	60	52	1.24	20	12	4915 200	52	2345.2
1.096	120	1000	1.085	50	500	48	38	1.24	16	10	2359 296	48	987.4

factor. The values of λ were a function of $dh_{\min}$, $dh_{\max}$, the total number of cells and the distance from the source to the model boundaries. The cell sizes were chosen finer near the source in order to better accommodate for the rapid variation of the EM fields in that region. The values of λ were smaller in the domain of interest, while they were larger in the air layer and in the extended domain. Table 2 specifies five different grids used to discretize the domain of interest and extended domain by listing the corresponding λ values, the minimum and maximum cell sizes in the domain of interest, the number of cells and resulting number of unknowns. In the extended domain, the minimum cell sizes are equal to the corresponding maximum cell sizes in the domain of interest and the maximum cell size is 4000 m. The air layer was discretized with 20 horizontal layers of cells with $\lambda = 1.31$ (in the z-direction) and minimum cell thickness of 60 m at the air-water interface.

We first consider the VTI model ($\theta = \phi = 0^\circ$) of Fig. 7. The multigrid preconditioned BiCGStab(2) solver needed 70 iterations to allow the relative residual norm to become smaller than 10^{-8} for the linear system with the largest number of unknowns over 56 million (top row in Table 2). The corresponding linear system solution time was 617 minute. We notice that the convergence rate of the solver became significantly slower than for the deep-water model, *cf.* Table 1. The reason for the slow convergence is ill conditioning of the matrix resulting from large aspect ratios of the cell sizes in the air layer and thick boundary paddings. The very high resistivity in the air layer is an additional reason—this gives a large null-space to the 3-D curl–curl operator (Mulder 2006).

Fig. 8(a) shows the amplitude (left) and phase (right) responses for E_x (black line) and E_z (red line) at 0.5 Hz along an inline receiver line located at the seabed. Fig. 8(b) (black and red lines) shows the

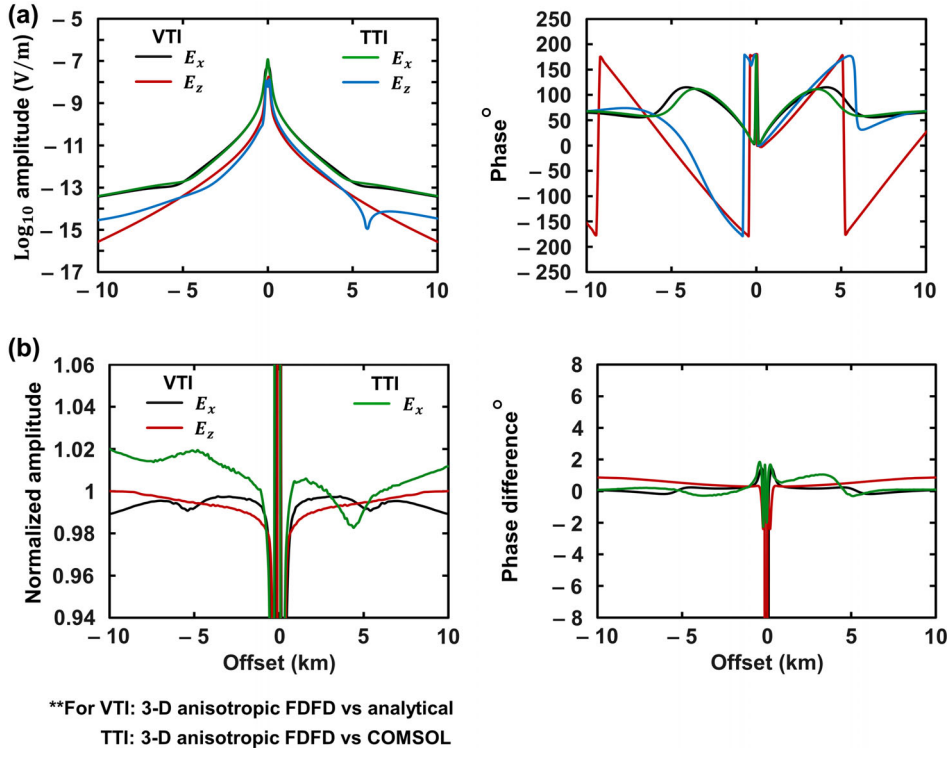

Figure 8. (a) Amplitude (left-hand panel) and phase (right-hand panel) responses of E_x and E_z at 0.5 Hz for the shallow-water VTI and TTI models of Fig. 7 computed using the developed anisotropic 3-D FDFD method. (b) Normalized amplitude (left-hand panel) and phase difference (right-hand panel) between the responses shown in (a) and a semi-analytical solution (Løseth & Ursin 2007) for the VTI model, and between E_x shown in (a) and E_x computed using COMSOL Multiphysics software for the TTI model.

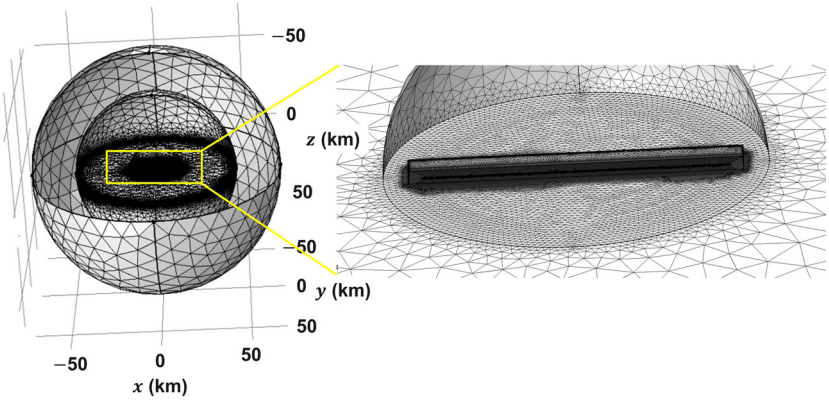

Figure 9. Mesh used to discretize the resistivity model of Fig. 7 (along with the air layer and boundary paddings) to compute a numerical solution using COMSOL. It has three spheres with radii of respectively 15, 45 and 70 km, where the element sizes increase from innermost to outermost spheres. The discretization of the domain of interest is included in the innermost sphere. Furthermore, there is a cylinder with radius 1.5 km and length 26 km in the innermost sphere containing the region where the source and receivers are located and having the finest discretization. The total number of unknowns for this mesh is ∼9.4 million.

normalized amplitudes (left) and phase differences (right) between the responses shown in (a) and a semi-analytical solution (Løseth & Ursin 2007) for the shallow-water VTI model. We see that except for the responses that are very close to the source position, the field amplitudes differ at most by 1 per cent and the phases at most by 0.9°. The average relative errors computed using eq. (30) are 0.6 and 1 per cent, respectively, for E_x and E_z. Here $\eta = 5 \times 10^{-16}$ Vm^{-1} was chosen to calculate these errors. This implies that the developed anisotropic 3-D FDFD code provides very accurate results also for the shallow-water VTI case.

We now assume that the anisotropic layers (above and below the isotropic reservoir) in the model of Fig. 7 have tilted anisotropy with the anisotropic dip angle $\theta = -20°$ and strike angle $\phi = 0°$. Fig. 8(a) shows the amplitude (left) and phase (right) responses for E_x (green line) and E_z (blue line) at 0.5 Hz computed for this shallow-water TTI model and plotted together with the above shallow-water VTI model responses. Fig. 8(b) (green line) shows the normalized amplitude (left) and phase difference (right) between E_x shown in (a) and E_x computed using COMSOL software (with the mesh displayed in Fig. 9) for the TTI model. This shows that except for the response that is very close to the source position, the field amplitudes differ at most by 2 per cent and the phases at most by 1°, and the average relative difference (computed similarly as in the previous cases) is 1.4 per cent. The number of iterations and run-time for the iterative solver was almost the same as for the VTI model.

Note that we did not present the same comparison for the E_z component for the TTI model because there was a significant difference between E_z computed using the anisotropic 3-D FDFD and using COMSOL. We therefore tested the accuracy of COMSOL results for the shallow-water VTI model and found that they were quite accurate for E_x (within 1.5 per cent) but they exhibited significant errors for E_z. This could be due to improper handling of the discontinuity in E_z caused by a sharp conductivity contrast at the interface between the conductive seawater and resistive formation. In order to avoid such difficulties for benchmarking results of the future development, we include a Table A1 in Appendix with the numerical values of E_x and E_z for the shallow-water TTI model (plotted in Fig. 8a) along an inline receiver line (on the seabed) with the receiver spacing of 1 km from $x = -10$ km to +10 km.

Table 2 shows how the performance of the multigrid preconditioned BiCGStab(2) solver depends on the system size in the case of shallow water. Similar to the deep-water case, the solution time increases approximately linearly with the number of unknowns that here varies from 2.3 to 56 million. We again notice that the solver converges slightly faster (needs fewer iterations) for smaller systems, though this dependence is pretty weak.

3-D models and titled anisotropy effect on CSEM responses

In this section, we consider 3-D TTI earth models and compare the developed anisotropic 3-D FDFD simulation results with the results obtained using an anisotropic 3-D FDFD algorithm developed by Davydycheva *et al*. (2003). The latter algorithm is based on the FD discretization of Maxwell's equations on the Lebedev grid, and the resulting linear system is solved using the spectral Lanczos decomposition method. Recently, this algorithm has been used by Davydycheva & Frenkel (2013) to study the effect of tilted anisotropy on synthetic CSEM responses by using complex 3-D TTI earth models with synclinal and anticlinal structures in a VTI background. We will examine the same effect and reproduce the results with our anisotropic 3-D FDFD algorithm.

Following Davydycheva & Frenkel (2013), we built three deep-water 3-D models with: (1) only a VTI background (Fig. 10a), (2) a TTI anticlinal structure in a VTI background (Fig. 10b) and (3) a TTI synclinal structure in a VTI background (Fig. 10c). For all models, the EM fields are excited by an x-oriented HED with frequencies of 0.25, 0.5 and 1 Hz towed 30 m above the seabed. The responses are recorded along an inline receiver line located at the flat seabed.

Model with VTI background

Let us consider the 3-D deepwater earth model with a reservoir in a VTI subsurface depicted in Fig. 10(a). The transverse and normal resistivities of the background subsurface are, respectively, $\rho_T = 1$ Ωm and $\rho_N = 2$ Ωm, while the strike and dip angles are zero, $\phi = \theta = 0°$. The reservoir with isotropic resistivity of 20 Ωm is located at 1.5 km below the seabed and has a dimension

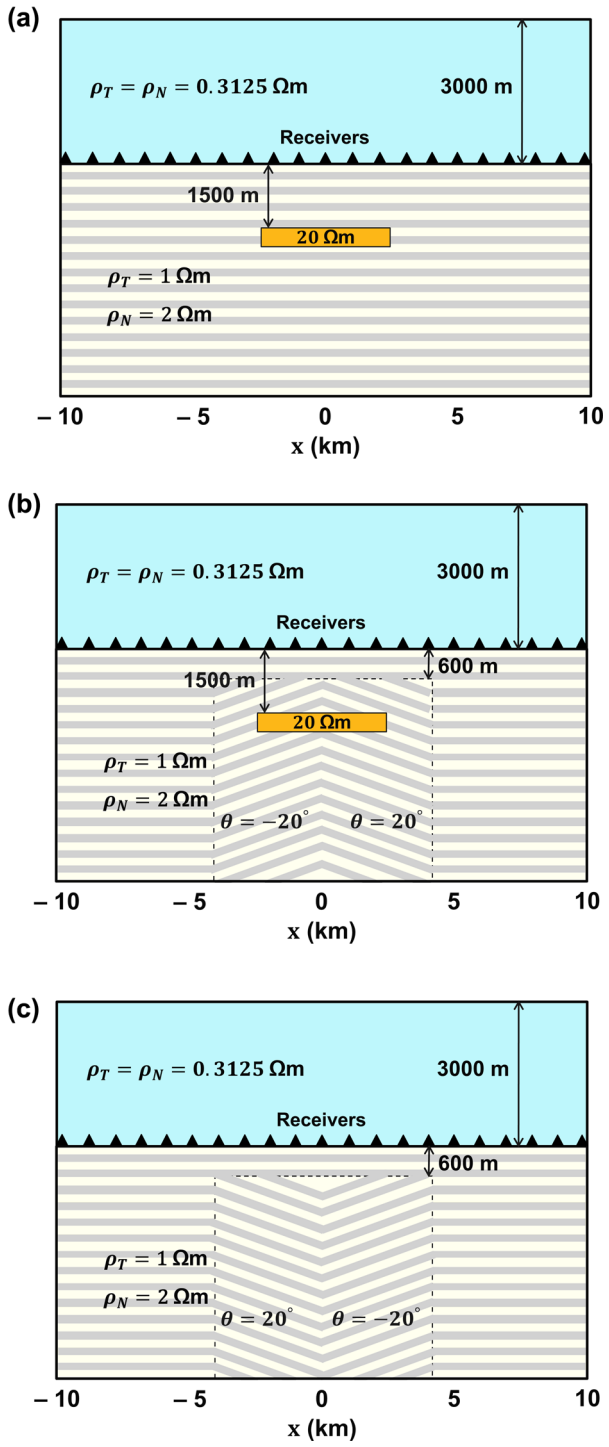

Figure 10. Vertical cross-section of 3-D deep-water earth models with: (a) a reservoir in a VTI subsurface, (b) a reservoir in a TTI anticline and (c) a TTI syncline. The overburden and background of the anticline and syncline are the same VTI media as the subsurface of the model in (a).

of $5 \times 5 \times 0.1$ km^3. The same model but without the reservoir is called 'the reference VTI model' in this paper.

Fig. 11(a) shows the absolute amplitude responses of E_x plotted as a function of source–receiver ($T_x - R_x$) midpoint positions at three $T_x - R_x$ offsets: 4, 6 and 8 km. These responses are calculated using the developed Lebedev grid based anisotropic multigrid solver (solid lines) and a Yee grid based VTI code (filled circles) from Jaysaval *et al*. (2014). From these plots, we observe that both methods give almost identical results. Fig. 11(b) shows normalized amplitudes with respect to the amplitude responses for the reference VTI model. It is clear from Fig. 11(b) that the presence of the reservoir in VTI subsurface causes significant increase in the amplitudes (as compared to the background), specifically at longer offsets. The absolute and normalized amplitude plots showing the effect of the reservoir in the VTI background are visibly identical to the ones presented in fig. 4 of Davydycheva & Frenkel (2013).

Model with TTI anticlinal structure

The 3-D deepwater earth model with a reservoir in a TTI symmetric-anticlinal structure is shown in Fig. 10(b). The anticline is a 2-D structure with the strike parallel to the y-axis and is symmetric with respect to the reservoir centre. The anticline is modelled as two bulk-tilted anisotropic structures corresponding to its two limbs (or flanks), each having the horizontal width of 4 km in the x-direction. The strike angle $\phi = 0^\circ$ for both limbs whereas the dip angle $\theta = -20^\circ$ for the left limb and $\theta = 20^\circ$ for the right limb. The top of the anticline is located at 0.6 km below the seabed. The overburden and background are the same VTI media as in the previous 3-D model. The transverse and normal resistivities of the tilted layers of both limbs are the same as in the VTI background: $\rho_T = 1\ \Omega$m and $\rho_N = 2\ \Omega$m, respectively.

We first consider the model in Fig. 10(b) without the reservoir and observe the effect of only the TTI anticlinal structure on the CSEM responses. For this model, Fig. 12(a) shows the absolute amplitudes and Fig. 12(b) the normalized amplitudes with respect to the reference VTI model responses for E_x. It is evident that the anticlinal structure causes a significant drop in the amplitudes up to 40 per cent. This implies that the anticlinal structure can mask responses of the highly resistive reservoir, which caused the opposite effect, that is elevation in amplitudes (Fig. 11). These plots for the anticlinal structure responses on CSEM data look visibly the same as the ones presented in fig. 5 (bottom row) of Davydycheva & Frenkel (2013). This match gives confidence in the accuracy of the developed anisotropic 3-D FDFD algorithm.

Fig. 13 shows the absolute amplitudes and normalized amplitudes with respect to the reference VTI model responses for E_x for the model in Fig. 10(b), and thus illustrates a combined effect of the anticline structure and reservoir. Fig. 13(b) shows that at longer offsets, the combined effect of the anticlinal structure and reservoir is observed in which both cause nearly similar magnitude of the amplitude deviations from the background levels, but in the opposite directions, and hence they largely cancel each other. The observed effect also looks visibly the same as the one presented in fig. 5 (top row) of Davydycheva & Frenkel (2013).

Model with TTI synclinal structure

The 3-D deepwater earth model with a TTI symmetric-synclinal structure is shown in Fig. 10(c). The syncline is also a 2-D structure with the strike parallel to the y-axis and is modelled as two bulk-tilted anisotropic structures corresponding to its two limbs, each having the horizontal width of 4 km in the x-direction. The resistivities and strike angle of the tilted layers of both limbs are the same as of the anticline limbs in Fig. 10(b). In the syncline, the left limb has $\theta = 20^\circ$, while the right limb has $\theta = -20^\circ$. The

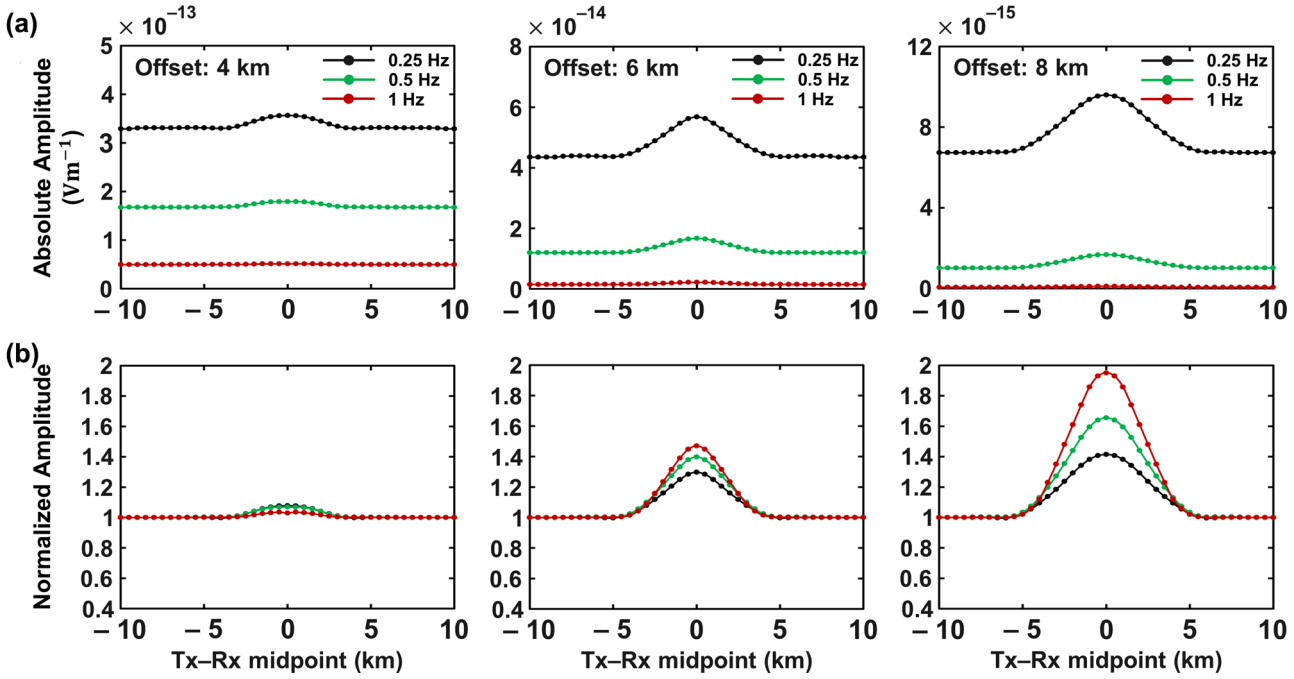

Figure 11. (a) Absolute amplitude responses of E_x at 0.25, 0.5 and 1 Hz for the 3-D model with a reservoir in VTI subsurface (Fig. 10a) plotted as a function of source–receiver ($T_x - R_x$) midpoint positions at three $T_x - R_x$ offsets: 4, 6 and 8 km. They are calculated using anisotropic 3-D FDFD (solid lines) code and a Yee grid based VTI FDFD (filled circles) code from Jaysaval *et al*. (2014). (b) Normalized amplitudes with respect to the amplitude responses for the reference VTI model (the model in Fig. 10a without the reservoir).

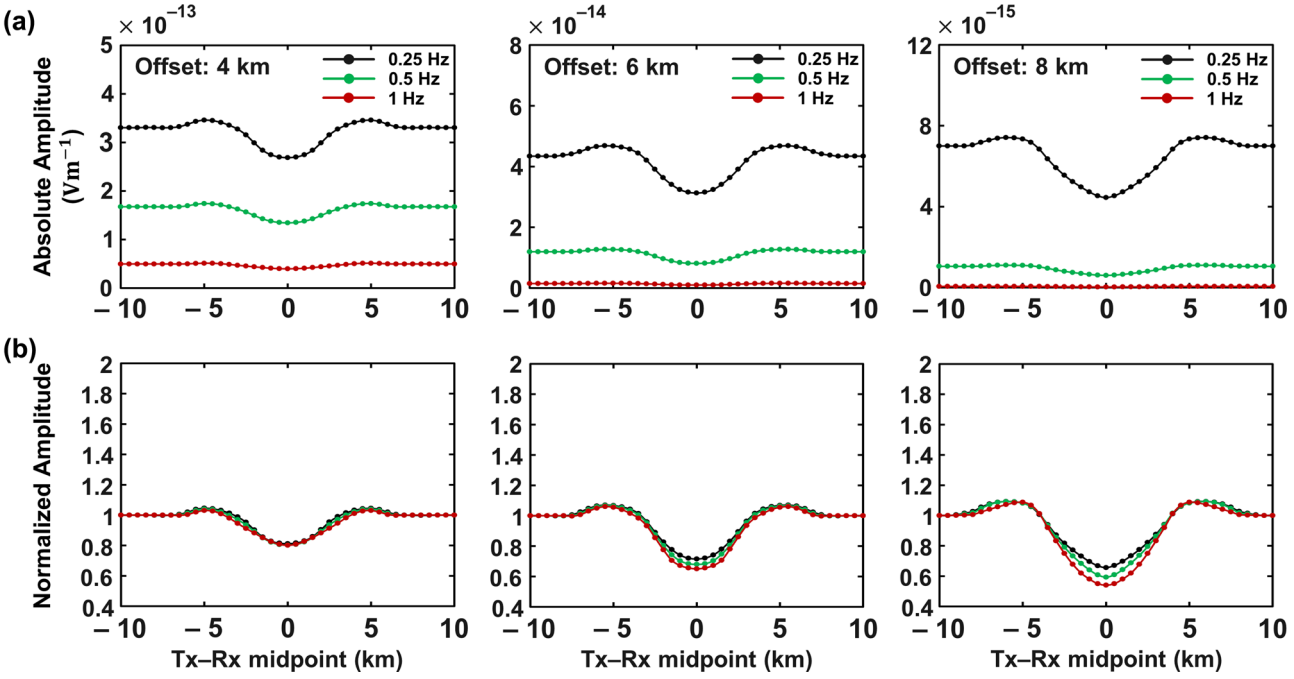

Figure 12. (a) Absolute amplitude responses of E_x at 0.25, 0.5 and 1 Hz for the 3-D model with a TTI anticline (without the reservoir) of Fig. 10(b) calculated using the developed anisotropic 3-D FDFD method. (b) Normalized amplitudes with respect to the amplitude responses for the reference VTI model.

overburden, background and location of the top of the syncline are the same as of the anticline in the previous model.

Fig. 14(a) shows the absolute amplitudes and Fig. 14(b) the normalized amplitudes with respect to the reference VTI model responses for E_x for the model with the syncline. It is clear that the synclinal structure causes an elevation in the amplitude when the source–receivers midpoint positions are above its central part. Hence, this structural effect can be misinterpreted as a highly resistive hydrocarbon reservoir if CSEM data are to be analysed using VTI assumption of the subsurface anisotropy. The synclinal structure effect on CSEM data again looks the same as the effect observed in fig. 6 (bottom row) of Davydycheva & Frenkel (2013).

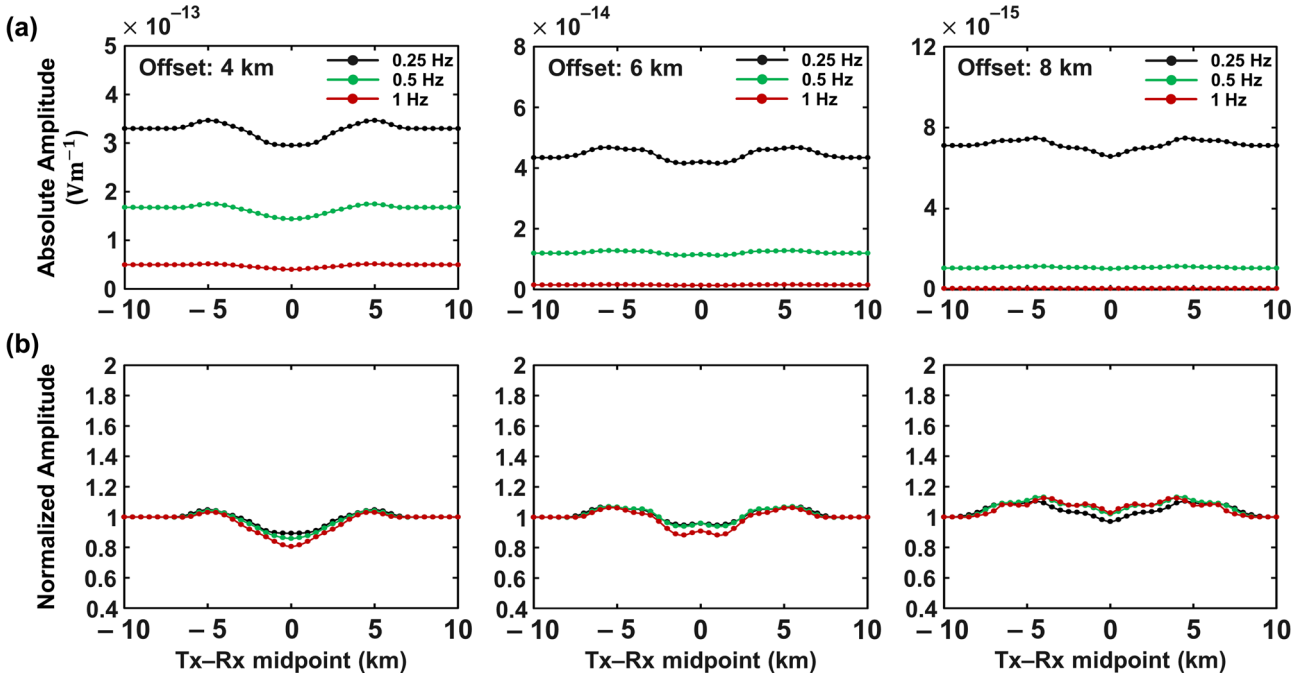

Figure 13. The same as Fig. 12, but for the 3-D model with a reservoir in the anticline (Fig. 10b).

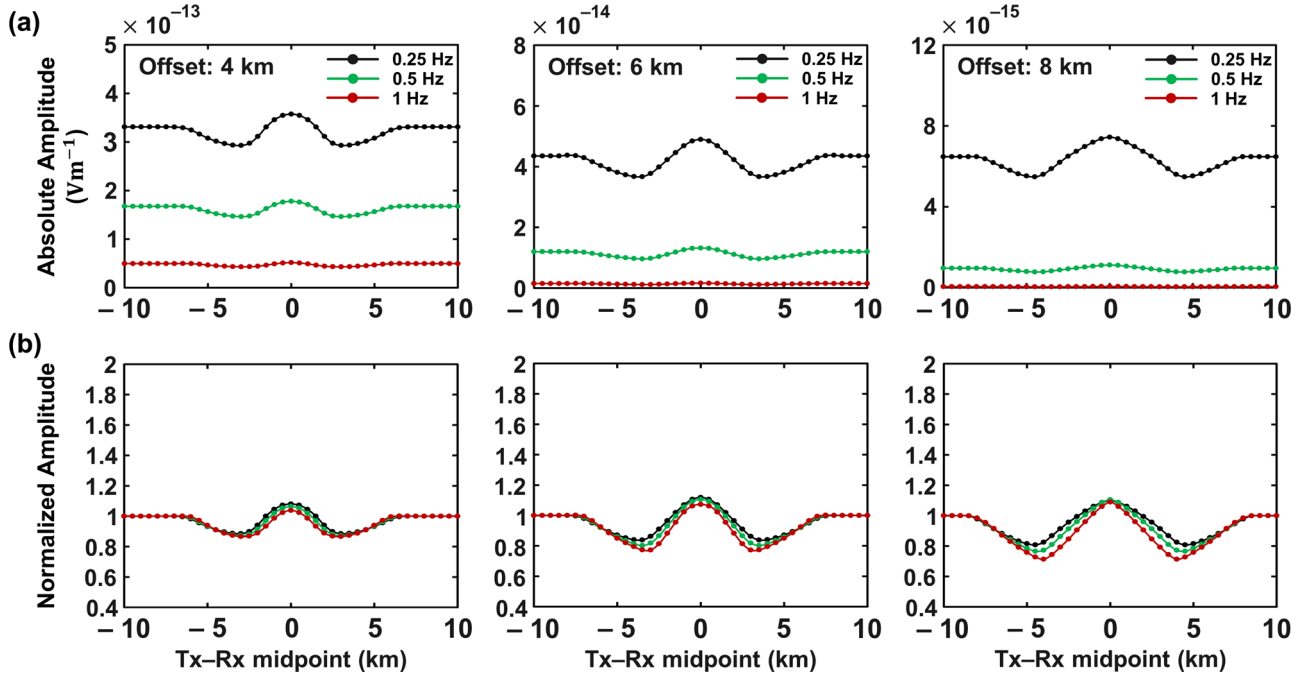

Figure 14. (a) Absolute amplitude responses of E_x at 0.25, 0.5 and 1 Hz for the 3-D model with a TTI syncline of Fig. 10(c) calculated using the developed anisotropic 3-D FDFD method. (b) Normalized amplitudes with respect to the amplitude responses for the reference VTI model.

PRELIMINARY INVERSION EXPERIMENTS

In the previous section, we observed the effect of anticlinal and synclinal structures on the CSEM responses. It was demonstrated that anticlinal structures could significantly reduce the inline electric field amplitude. This effect persists even in the presence of a highly resistive reservoir, and hence can mask the reservoir response. On the other hand, the synclinal structure causes an increase in the electric field amplitude when the source–receivers midpoint positions are above its central part. This effect can be misinterpreted as a resistive anomaly due to, for example, a hydrocarbon reservoir if CSEM data are analysed using VTI anisotropy assumption. A possible reason of such effects could be based on the fact that the electric field is more sensitive to ρ_N if the electric field lines align more towards the bed-normal direction and to ρ_T if they align in the bed-parallel direction. Since $\rho_N > \rho_T$ and higher resistivity implies less attenuation or larger field amplitudes, we would expect an increase in the amplitude if the tilted layers are oriented such that the electric field lines have larger components in the bed-normal direction, and a decrease if the electric field lines tend to

align in the bed-parallel direction. However, one would need to plot the field lines in the subsurface to see whether this argumentation can explain the observed effects for the anticline and syncline structure.

The VTI assumption is quite widespread for inversion and interpretation of CSEM data. Therefore, it is interesting to study whether the presence of anticlinal or synclinal structures would produce artefacts in VTI inversion results and whether they can be removed by running a TTI inversion.

In this section, we perform a 2.5-D CSEM inversion study for the simulation data computed for the models with anticlinal and synclinal structures of Fig. 10. The inversion is based on a Gauss–Newton optimization method and is described in Hansen & Mittet (2009). We present inversion results obtained using both VTI inversion and a basic TTI inversion scheme. The difference in these two schemes is assumed to be only in the use of forward solver: the VTI inversion uses a forward solver that handles VTI anisotropy, while the TTI inversion uses a forward solver that can also handle the TTI anisotropy of the models. The true dip θ and strike ϕ angles are assumed to be known and are kept fixed in the TTI inversion. We stress that the latter is a simplified TTI inversion scheme that, although useful to illustrate the importance of dipping anisotropy via synthetic examples, lacks the necessary functionality for inverting general field data. Full TTI inversion is discussed further at the end of this section but is, otherwise, beyond the scope of this paper.

In both inversions, inline electric field E_x data was used for 21 receivers, which are placed on the seabed along a line in the central part of the model with 1 km spacing from $x = -10$ to $+10$ km. A HED source is towed 30 m above the seabed and data are recorded for source–receiver offsets up to 10 km. Note that the 2.5-D assumption along a receiver line in the central part of the model holds fairly well because the reservoir is sufficiently wide (5 km) and the anticline and syncline are indeed 2-D structures. The forward engine used in the inversion is a 2.5-D TTI version of the modified time-domain code presented by Maaø (2007) and is based on the Yee grid. It is therefore very different from the forward engine used to generate data going into inversion. These data were also contaminated with a multiplicative noise of 1 per cent and an additive noise of 10^{-16} V m^{-1}.

Let us consider the simulation data presented in Fig. 11 for frequencies 0.25 and 0.5 Hz for the model with a reservoir in the VTI background (Fig. 10a). For these datasets, we ran only the VTI inversion since there is no tilted anisotropy in the subsurface. The VTI inversion was started using a half-space model with correct background resistivities $\rho_N = 2$ Ωm and $\rho_T = 1$ Ωm. Figs 15(a) and (b) show the final VTI inversion results, respectively, for ρ_N and ρ_T. The inversion accurately imaged the true resistivity model shown in Fig. 10(a): it produced a clear resistive anomaly at about 1.5 km below the seabed.

We now consider the simulation data presented in Fig. 13 for frequencies 0.25 and 0.5 Hz for the model with a reservoir in the anticlinal structure (Fig. 10b). We ran both VTI and TTI inversions for these datasets using the same half-space starting model as in the previous inversion. For TTI inversion, the values of θ and ϕ for the start model were chosen to be the same as in the true model with the anticline, while for the VTI inversions both angles were set to zero.

Figs 16(a) and (c) show the final VTI inversion results, respectively, for ρ_N and ρ_T. It is clear that the VTI inversion was not able to image the reservoir: the inverted ρ_N model does not show any anomaly. The ρ_T model has a weak resistive structure, but its shape does not match that of the reservoir. As discussed before, the reason

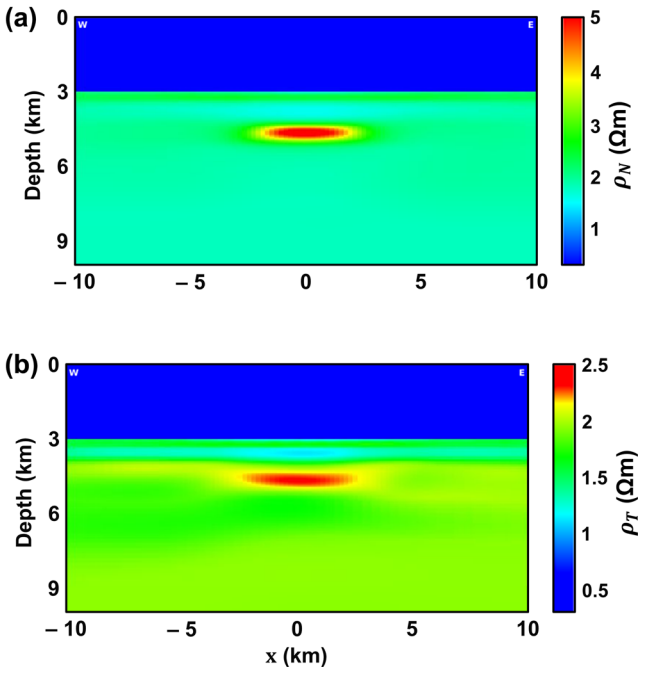

Figure 15. VTI inversion results for simulation data at 0.25 and 0.5 Hz for the 3-D model with a reservoir in the VTI subsurface (Fig. 10a): the reservoir is accurately imaged in the normal (a) and transverse (b) resistivities.

for such inversion results is the combined effect of the reservoir and anticlinal structure in which the amplitude responses remain close to the background level (see Fig. 13). At the same time, the TTI inversion delivered much better results, see Figs 16(b) and (d), respectively, for ρ_N and ρ_T. The true resistivity model of Fig. 10(b) is reconstructed very accurately by the TTI inversion: there is a clear resistive anomaly in the inverted resistivity images located at about 1.5 km below the seabed. Note that the VTI inversion converged to a smaller final misfit and used fewer iterations than the TTI inversion, that is the convergence plots do not give any indications that the VTI results might be wrong.

Finally, we consider the simulation data presented in Fig. 14 for frequencies 0.25 and 0.5 Hz for the model having a synclinal structure in the subsurface (Fig. 10c), but no reservoir. We ran both VTI and TTI inversions for these datasets using a half-space start model with resistivities $\rho_N = 2.1$ Ωm and $\rho_T = 0.9$ Ωm, which are 5–10 per cent different from the true background resistivities. For TTI inversion, the start model had the true values of θ and ϕ, while for VTI inversion both angles were zero. Figs 17(a) and (c) show the final VTI inversion results, respectively, for ρ_N and ρ_T. A highly resistive anomaly can be seen in the inverted resistivity ρ_N, despite the true model not having any resistive objects. This fictitious anomaly is the effect of synclinal structure that tends to elevate the electric field amplitude when the source–receivers midpoint positions are above its central part. This structural anomaly in the inversion results can be misinterpreted as a hydrocarbon reservoir. Figs 17(b) and (d) show the TTI inversion results, which are consistent with the true resistivity model and show no anomalies.

It is therefore clear that using VTI inversion to image the subsurface resistivity in complex tectonic areas can lead to severe inversion artefacts. We also have every indication that the application of TTI inversion is crucial to image the subsurface resistivity correctly in such areas. Here, we would like to mention that the TTI inversion scheme can be developed further to allow one to invert also for θ and ϕ. In practice, these angles can often be obtained from the existing

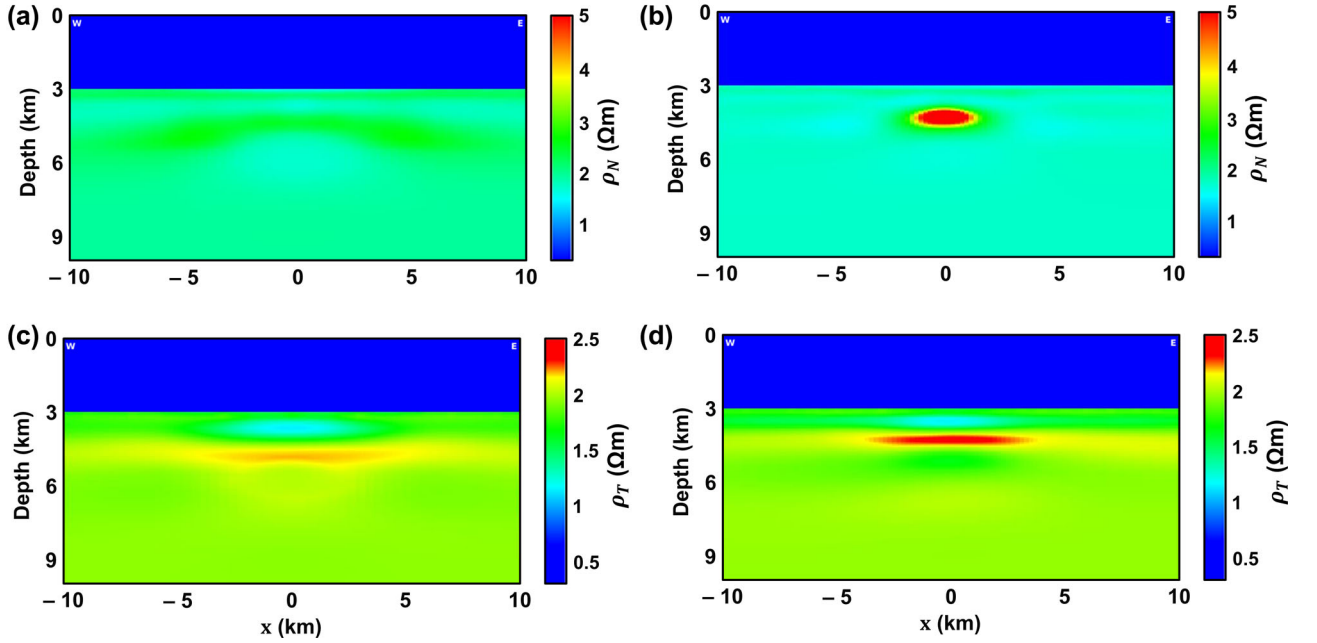

Figure 16. VTI (left-hand panel) and TTI (right-hand panel) inversion results for normal (top panel) and transverse (bottom panel) resistivities using simulation data at 0.25 and 0.5 Hz for the 3-D model with a reservoir in the anticline (Fig. 10b). VTI inversion failed to image the reservoir since it got masked by the anticline response. TTI inversion, however, recovered it pretty accurately.

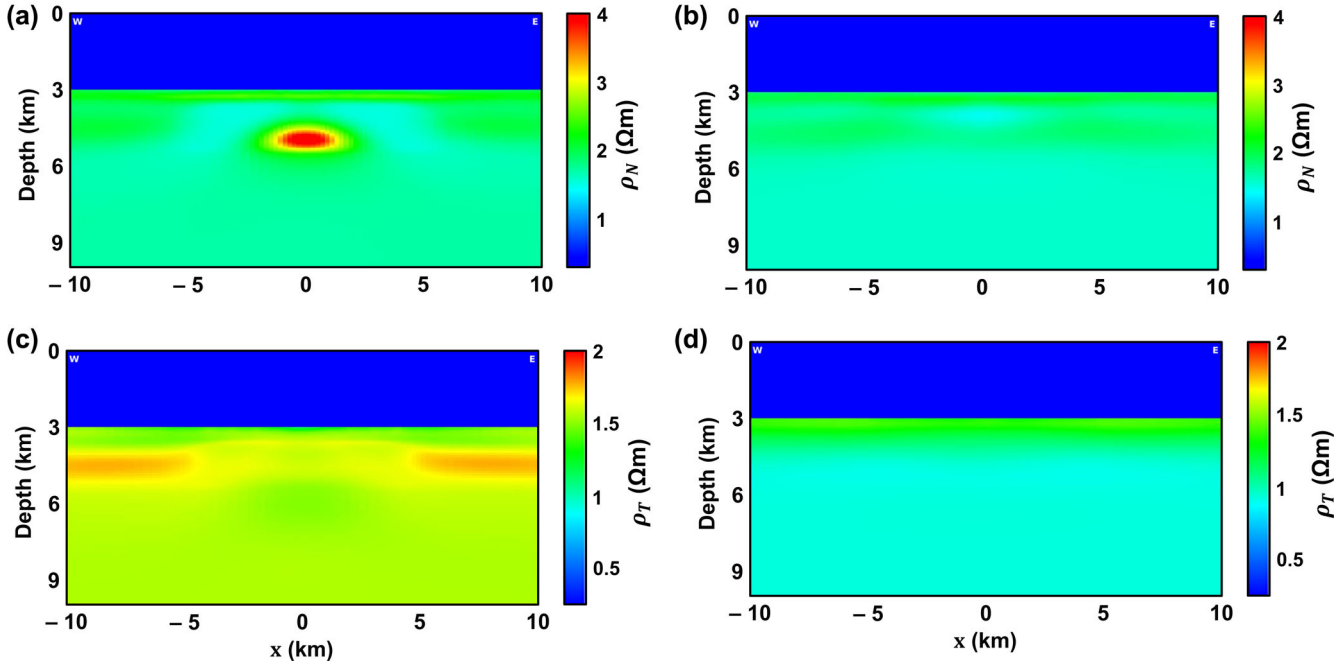

Figure 17. VTI (left-hand panel) and TTI (right-hand panel) inversion results for normal (top panel) and transverse (bottom panel) resistivities using simulation data at 0.25 and 0.5 Hz for the 3-D model with a syncline (Fig. 10c). VTI inversion places a false anomaly at the middle of the syncline, while TTI inversion does not produce any artefacts.

seismic data that show the subsurface structures. However, if this structural information is unavailable or inaccurate, then a full TTI inversion will be needed. Moreover in our simplified TTI inversion scheme, the gradient and Hessian were computed from the misfit derivatives with respect to the vertical and horizontal resistivities (rather than ρ_N and ρ_T), hence the model update was somewhat inaccurate. Nevertheless, even with this imperfect model update, the TTI inversion demonstrated a dramatic improvement over the VTI inversion in the presence of tilted structures.

An upcoming publication (Hansen *et al*. 2016) presents a TTI inversion that includes all functionality discussed above and is extended to the 3D case. This paper further supports our conclusions that (i) a VTI inversion may result in imaging artifacts in the presence of dipping structures, and (ii) these artifacts disappear if the TTI anisotropy is taken into account. Besides, it demonstrates that a TTI inversion using a forward solver based on the Lebedev grid can be successfully applied not only to synthetic but also to field data, on an example of a

CSEM survey acquired over the Perdido fold belt in the Gulf of Mexico.

CONCLUSIONS

We developed a Lebedev-grid based FDFD method for numerical modelling of CSEM fields in 3-D media with general electric anisotropy. A BiCGStab(2) solver with a multigrid preconditioner was used to solve the resulting system of linear equations. We observed that the linear system solution time increased approximately linearly with the number of unknowns. A synthetic inversion study revealed that ignoring TTI anisotropy in complex 3-D models with anticlinal and synclinal structures can lead to misleading resistivity images. It was found that the VTI inversion of data corresponding to a model with a reservoir in an anticline resulted in a resistivity image showing no anomaly. On the other hand, the VTI inversion of data corresponding to a model with a syncline resulted a false resistive anomaly in the inverted resistivity image, despite the true model not having any resistive bodies. By contrast, when inversion uses the proposed TTI forward code, the produced resistivity images become consistent with the true models. We therefore believe that the developed anisotropic 3-D FDFD modelling code along with a proper inversion scheme will help improve imaging of the subsurface resistivity in dipping environments, and thereby increase drilling success rates for hydrocarbon discoveries.

ACKNOWLEDGEMENTS

We thank EMGS for giving permission to publish the results and the Research Council of Norway for supporting this work through Petromaks program. We express our gratitude to Dr Anders Malthe-Sørenssen and Dr Joakim Bergli for helpful and inspiring suggestions, and the MUMPS team for proving the direct solver. We wish to express our gratitude to the editor, Dr Ute Weckmann, and two anonymous reviewers for their careful reading, suggestions and constructive comments.

REFERENCES

Alcocer, J.A.E., García, M.V., Soto, H.S., Baltar, D., Paramo, V.R., Gabrielsen, P. & Roth, F., 2013. Reducing uncertainty by integrating 3D CSEM in the Mexican deep-water exploration workflow, *First Break,* **31,** 75–79.

Arnold, D.N., Falk, R.S. & Winther, R., 2000. Multigrid in *H* (div) and; *H* (curl), *Numer. Math.,* **85,** 197–217.

Aruliah, D.A. & Ascher, U.M., 2002. Multigrid preconditioning for Krylov methods for time-harmonic Maxwell's equations in three dimensions, *SIAM J. Sci. Comput.* **24**(2), 702–718.

Börner, R.-U., Ernst, O.G. & Güttel, S., 2015. Three-dimensional transient electromagnetic modelling using Rational Krylov methods, *Geophys. J. Int.,* **202**(3), 2025–2043.

Briggs, W.L., Henson, V.E. & McCormick, S.F., 2000. *A Multigrid Tutorial,* SIAM.

Constable, S., 2010. Ten years of marine CSEM for hydrocarbon exploration, *Geophysics,* **75**(5), A67–A81.

da Silva, N.V., Morgan, J.V., Macgregor, L. & Warner, M., 2012. A finite element multifrontal method for 3D CSEM modeling in the frequency domain, *Geophysics,* **77**(2), E101–E115.

Davydycheva, S. & Druskin, V., 1999. Staggered grid for Maxwell's equations in arbitrary 3D inhomogeneous anisotropic media, in *Three-Dimensional Electromagnetics,* pp. 138–145, eds Oristaglio, M. & Spies, B., Society of Exploration Geophysicists.

Davydycheva, S. & Frenkel, M.A., 2010. Review of 3D EM modeling and interpretation methods for triaxial induction and propagation resistivity well logging tools, in *PIERS Proceedings,* Cambridge, USA, pp. 390–396.

Davydycheva, S. & Frenkel, M.A., 2013. The impact of 3D tilted resistivity anisotropy on marine CSEM measurements, *Leading Edge,* **32**(11), 1374–1381.

Davydycheva, S., Druskin, V. & Habashy, T., 2003. An efficient finite-difference scheme for electromagnetic logging in 3D anisotropic inhomogeneous media, *Geophysics,* **68**(5), 1525–1536.

Druskin, V.L., Knizhnerman, L.A. & Lee, P., 1999. New spectral Lanczos decomposition method for induction modeling in arbitrary 3-D geometry, *Geophysics,* **64**(3), 701–706.

Eidesmo, T., Ellingsrud, S., MacGregor, L.M., Constable, S., Sinha, M.C., Johansen, S., Kong, F.N. & Westerdahl, H., 2002. Sea bed logging (SBL), a new method for remote and direct identification of hydrocarbon filled layers in deepwater areas, *First Break,* **20,** 144–152.

Ellingsrud, S., Eidesmo, T., Sinha, M.C., MacGregor, L.M. & Constable, S., 2002. Remote sensing of hydrocarbon layers by seabed logging (SBL): results from a cruise offshore Angola, *Leading Edge,* **21,** 972–982.

Fanavoll, S., Ellingsrud, S., Gabrielsen, P.T., Tharimela, R. & Ridyard, D., 2012. Exploration with the use of EM data in the Barents Sea: the potential and the challenges, *First Break,* **30,** 89–96.

Gutknecht, M.H., 1993. Variants of BiCGStab for matrices with complex spectrum, *SIAM J. Sci. Stat. Comput.,* **14**(5), 1020–1033.

Hansen, K.R. & Mittet, R., 2009. Incorporating seismic horizons in inversion of CSEM data, in *Proceedings of the 79th SEG Annual International Meeting,* Houston, USA, pp. 694–698.

Hansen, K.R., Panzner, M., Shantsev, D. & Mittet, R., 2016. TTI inversion for marine CSEM data, in *Proceedings of the 86th SEG Annual International Meeting,* Dallas, USA.

Hesthammer, J., Stefatos, A., Boulaenko, M., Fanavoll, S. & Danielsen, J., 2010. CSEM performance in light of well results, *Leading Edge,* **29**(1), 34–41.

Jaysaval, P., Shantsev, D. & Kethulle de Ryhove, S., 2014. Fast multimodel finite-difference controlled-source electromagnetic simulations based on a Schur complement approach, *Geophysics,* **79**(6), E315–E327.

Jaysaval, P., Shantsev, D.V. & de la Kethulle de Ryhove, S., 2015. Efficient 3-D controlled-source electromagnetic modelling using an exponential finite-difference method, *Geophys. J. Int.,* **203**(3), 1541–1574.

Koldan, J., Puzyrev, V., de la Puente, J. & Houzeaux, G., 2014. Algebraic multigrid preconditioning within parallel finite-element solvers for 3-D electromagnetic modelling problems in geophysics, *Geophys. J. Int.,* **197,** 1442–1458.

Lebedev, V.I., 1964. Difference analogies of orthogonal decompositions of basic differential operators and some boundary value problems. I, *Soviet Comput. Maths. Math. Phys.,* **4,** 449–465.

Li, Y. & Dai, S., 2011. Finite element modeling of marine controlled-source electromagnetic responses in two-dimensional dipping anisotropic conductivity structures, *Geophys. J. Int.,* **185,** 622–636.

Liu, Y. & Yin, C., 2014. 3D anisotropic modeling for airborne EM systems using finite-difference method, *J. appl. Geophys.,* **109,** 186–194.

Løseth, L.O. & Ursin, B., 2007. Electromagnetic fields in planarly layered anisotropic media, *Geophys. J. Int.,* **170,** 44–80.

Maaø, F.A., 2007. Fast finite-difference time-domain modelling for marine subsurface electromagnetic problems, *Geophysics,* **72,** 19–23.

Martí, A., 2014. The role of electrical anisotropy in magnetotelluric responses: from modelling and dimensionality analysis to inversion and interpretation, *Surv. Geophys.,* **35,** 179–218.

Mulder, W.A., 2006. A multigrid solver for 3D electromagnetic diffusion, *Geophys. Prospect.,* **54,** 633–649.

Nauta, M., Okoniewski, M. & Potter, M., 2013. FDTD method on a Lebedev grid for anisotropic materials, *IEEE Trans. Antennas Propag.,* **61**(6), 3161–3171.

Newman, G.A. & Alumbaugh, D.L., 1995. Frequency-domain modeling of airborne electromagnetic responses using staggered finite differences, *Geophys. Prospect.,* **43,** 1021–1042.

Newman, G.A. & Alumbaugh, D.L., 2002. Three-dimensional induction logging problems. Part 2: A finite-difference solution, *Geophysics,* **67**(2), 484–491.

Puzyrev, V. & Koric, S., 2015. 3D multi-source CSEM simulations: feasibility and comparison of parallel direct solvers, in *Proceedings of the 85th SEG Annual International Meeting,* New Orleans, USA, pp. 833–838.

Puzyrev, V., Koldan, J., Puente, J., Houzeaux, G., Vázquez, M. & Cela, J.M., 2013. A parallel finite-element method for three-dimensional controlled-source electromagnetic forward modelling, *Geophys. J. Int.,* **193**(2), 678–693.

Saad, Y., 2003. *Iterative Methods for Sparse Linear Systems,* SIAM.

Shantsev, D.V. & Maaø, F.A., 2015. Rigorous interpolation near tilted interfaces in 3-D finite-difference EM modelling, *Geophys. J. Int.,* **200**(2), 745–757.

Smith, J.T., 1996. Conservative modeling of 3-D electromagnetic fields. Part II: Biconjugate gradient solver and an accelerator, *Geophysics,* **61**(5), 1319–1324.

Streich, R., 2009. 3D finite-difference frequency-domain modeling of controlled-source electromagnetic data: direct solution and optimization for high accuracy, *Geophysics,* **74**(5), F95–F105.

Trottenberg, U., Oosterlee, C. & Schüller, A., 2001. *Multigrid,* Academic Press.

van der Vorst, H.A., 1992. BI-CGSTAB: a fast and smoothly converging variant of bi-CG for the solution of nonsymmetric linear systems, *SIAM J. Sci. Stat. Comput.,* **13**(2), 631–644.

Wang, T. & Fang, S., 2001. 3-D electromagnetic anisotropy modeling using finite differences, *Geophysics,* **66**(5), 1386–1398.

Weidelt, P., 1999. 3D conductivity models: implications of electrical anisotropy, in *Three-Dimensional Electromagnetics,* pp. 119–137, eds Oristaglio, M. & Spies, B., Society of Exploration Geophysicists.

Weiss, C.J. & Newman, G.A., 2002. Electromagnetic induction in a fully 3-D anisotropic earth, *Geophysics,* **67**(4), 1104–1114.

Wesseling, P., 1991. *An Introduction to Multigrid Methods,* John Wiley & Sons.

Yee, K., 1966. Numerical solution of initial boundary value problems involving Maxwell's equations in isotropic media, *IEEE Trans. Antennas Propag.,* **14,** 302–307.

APPENDIX: NUMERICAL VALUES OF THE EM FIELDS FOR THE SHALLOW-WATER TTI MODEL

In this appendix, we include a table of numerical values of the amplitude and phase responses of E_x and E_z at 0.5 Hz for the shallow-water TTI model. They are computed using the developed anisotropic 3-D FDFD code on the finest grid (top row in Table 2).

Table A1. Numerical values of amplitude and phase responses of E_x and E_z at 0.5 Hz for the shallow-water TTI model of Fig. 7.

	E_x		E_z			E_x		E_z	
Offsets	Amplitude (Vm^{-1})	Phase°	Amplitude (Vm^{-1})	Phase°	Offsets	Amplitude (Vm^{-1})	Phase°	Amplitude (Vm^{-1})	Phase°
−10 000	3.914E–14	67.518	2.845E–15	67.818	1000	1.282E–10	47.420	3.244E–11	27.472
−9000	5.450E–14	66.316	3.927E–15	70.877	2000	1.399E–11	83.718	3.775E–12	67.661
−8000	7.747E–14	63.492	6.051E–15	73.802	3000	2.535E–12	106.539	7.261E–13	106.274
−7000	1.090E–13	59.550	1.054E–14	71.720	4000	5.389E–13	108.198	1.577E–13	140.736
−6000	1.448E–13	58.334	1.965E–14	60.107	5000	1.942E–13	75.143	2.800E–14	169.108
−5000	1.911E–13	75.111	3.688E–14	35.722	6000	1.460E–13	58.504	2.230E–15	37.812
−4000	5.326E–13	108.893	7.139E–14	− 8.452	7000	1.096E–13	59.634	7.279E–15	40.550
−3000	2.527E–12	107.160	2.082E–13	− 75.795	8000	7.782E–14	63.527	6.490E–15	54.092
−2000	1.401E–11	84.096	1.160E–12	− 134.124	9000	5.473E–14	66.328	4.786E–15	63.399
−1000	1.290E–10	47.481	1.116E–11	− 172.884	10 000	3.930E–14	67.521	3.385E–15	68.316